



**Classifying Open-Air Target Measurements via  
Simulation-Trained Convolutional Neural  
Networks**

THESIS

Matthew M. Rofrano, B.S.E.E., Captain, USAF  
AFIT-ENG-MS-20-M-XXX

**DEPARTMENT OF THE AIR FORCE  
AIR UNIVERSITY**

**AIR FORCE INSTITUTE OF TECHNOLOGY**

**Wright-Patterson Air Force Base, Ohio**

DISTRIBUTION STATEMENT A  
APPROVED FOR PUBLIC RELEASE; DISTRIBUTION UNLIMITED.

The views expressed in this document are those of the author and do not reflect the official policy or position of the United States Air Force, the United States Department of Defense or the United States Government. This material is declared a work of the U.S. Government and is not subject to copyright protection in the United States.

AFIT-ENG-MS-20-M-XXX

Classifying Open-Air Target Measurements via Simulation Trained Convolutional  
Neural Networks

THESIS

Presented to the Faculty  
Department of Electrical and Computer Engineering  
Graduate School of Engineering and Management  
Air Force Institute of Technology  
Air University  
Air Education and Training Command  
in Partial Fulfillment of the Requirements for the  
Degree of Master of Science in Electrical Engineering

Matthew M. Rofrano, B.S.E.E., B.S.E.E.  
Captain, USAF

March 24, 2023

DISTRIBUTION STATEMENT A  
APPROVED FOR PUBLIC RELEASE; DISTRIBUTION UNLIMITED.

AFIT-ENG-MS-20-M-XXX

Classifying Open-Air Target Measurements via Simulation Trained Convolutional  
Neural Networks

THESIS

Matthew M. Rofrano, B.S.E.E., B.S.E.E.  
Captain, USAF

Committee Membership:

Robert F. Mills, Ph.D  
Chair

Charles XX. Macon,, Ph.D  
Member

DUNNO-SOME LO DUDE,, Ph.D  
Member

## Abstract

Current and historic tactics have leveraged the reduced detectability of Low Observable (LO) platforms and the confusion of decoys to complicate target identification and prosecution via radar. Ideally, adversary fires will be wasted engaging decoys, while destructive systems continue to advance on their targets. The ability to discern a threatening platform from a decoy will be crucial to increasing the survivability of friendly forces, and enable judicious use of fires. This project examines a potential solution for identifying a target in decoy-saturated airspace. A convolutional Neural Network is trained using RCS data for five targets. Targets are missile-surrogates that shares a similar fuselage, each with their own unique nose-cone. Training data is created by simulating the RCS response of each target using Altair's CADFeko Electromagnetic simulation quite. Data is captured over from 4.5 to 5.5 GHz, over 360 degrees of water-line azimuth angle, random-gaussian noise is applied to the frequency measurements of each angle, and normalized between 0 and 1. Normalized data is duplicated, labeled, and used to train the CNN. The trained network is tested for accuracy using measurement data collected at the Air Force Institute of Technologies compact radar cross section range. Measured targets are 1:1 copies of the simulation targets. The correlation of frequency measurements taken at each angle are correlated between the simulated, and measured targets to identify points of similarity and divergence in the resulting RCS response. These cross-correlation values are used to determine where miss-classifications occur in the CNN.

## Table of Contents

	Page
Abstract . . . . .	iv
List of Figures . . . . .	vii
List of Tables . . . . .	xi
I. Introduction . . . . .	1
1.1 Problem Background . . . . .	1
1.2 Research Objectives . . . . .	3
1.3 Document Overview . . . . .	3
II. Background and Literature Review . . . . .	4
2.1 Overview . . . . .	4
2.2 Simulation and Measurement Data . . . . .	5
2.2.1 Electromagnetic Wave Interaction . . . . .	5
2.2.2 Radar . . . . .	7
2.3 Measurement Calibration . . . . .	8
2.4 Instrumentation Quiet Zone . . . . .	10
2.5 Signal to Noise Performance . . . . .	10
2.6 Radar Cross Section . . . . .	12
2.7 Machine Learning Models . . . . .	15
2.7.1 Deep Learning . . . . .	16
2.7.2 Convolutional Neural Networks . . . . .	18
2.8 Optimizers and Augmentation . . . . .	22
2.9 Training . . . . .	22
2.9.1 Feature-Based Training . . . . .	23
2.9.2 Semi-Model Based Training . . . . .	23
2.9.3 Model-Based Training . . . . .	24
III. Methodology . . . . .	25
3.1 Overview . . . . .	25
3.2 Targets . . . . .	25
3.3 Measurement . . . . .	26
3.4 Simulation . . . . .	28
3.5 Data Processing . . . . .	29
3.5.1 Data Set Generation . . . . .	29
3.5.2 Data Augmentation . . . . .	30
3.5.3 Comparison . . . . .	30
3.6 Neural Network Development . . . . .	32
3.7 RCS Calculation . . . . .	32

	Page
IV. Results and Analysis .....	33
4.1 Preamble .....	33
4.2 Measurment Results .....	33
4.3 Simulation Results .....	34
4.4 Data Comparison .....	34
4.5 Model Evaluation .....	36
4.5.1 VGG-19 .....	36
4.5.2 VGG-16 .....	41
V. Conclusions .....	43
5.1 VGG-19 .....	43
5.2 VGG-16 .....	43
5.3 Future Work .....	43
Appendix A. Model Measurements .....	44
Appendix B. Models .....	46
Appendix C. Measurement Results .....	49
Appendix D. Simulation Results .....	54
Appendix E. Correlation Results .....	57
Appendix F. VGG-19 Results .....	67
Appendix G. VGG-16 Results .....	77
Bibliography .....	79
Acronyms .....	82

## List of Figures

Figure	Page
1 Air Launched Platform Comparison . . . . .	3
2 Project Overview . . . . .	4
3 Target missile . . . . .	13
4 Missile RCS data sample (Cut) . . . . .	14
5 Missile RCS data sample (Total) . . . . .	14
6 Missile RCS data, Angle Slice . . . . .	15
7 Perceptron node . . . . .	17
8 CNN overview . . . . .	19
9 Side and top view of the missile surrogate (Cad model) . . . . .	25
10 AFIT Compact Range Schematic . . . . .	27
11 Average Correlation vs SNR . . . . .	36
12 VGG-19 Model Testing, and Selection . . . . .	38
13 VGG-19 Siamese Network Performance . . . . .	39
14 VGG-19 Siamese Network Performance . . . . .	42
15 Simulation targets 1 and 2 . . . . .	46
16 Simulation targets 3 and 4 . . . . .	47
17 Simulation targets 3 and 4 . . . . .	48
18 Missile 1 ( <b>Test</b> ): RCS cut at 5 GHz. Vertical (tt) and Horizontal (pp) polarizations . . . . .	49
19 Missile 2 ( <b>Test</b> ): RCS cut at 5 GHz. Vertical (tt) and Horizontal (pp) polarizations . . . . .	50
20 Missile 3 ( <b>Test</b> ): RCS cut at 5 GHz. Vertical (tt) and Horizontal (pp) polarizations . . . . .	50

Figure	Page
21      Missile 4 ( <b>Test</b> ): RCS cut at 5 GHz. Vertical (tt) and Horizontal (pp) polarizations .....	51
22      Missile 5 ( <b>Test</b> ): RCS cut at 5 GHz. Vertical (tt) and Horizontal (pp) polarizations .....	51
23      Missile 1 ( <b>Test</b> ): Total RCS. Vertical (tt) and Horizontal (pp) polarizations .....	52
24      Missile 2 ( <b>Test</b> ): Total RCS. Vertical (tt) and Horizontal (pp) polarizations .....	52
25      Missile 3 ( <b>Test</b> ): Total RCS. Vertical (tt) and Horizontal (pp) polarizations .....	52
26      Missile 4 ( <b>Test</b> ): Total RCS. Vertical (tt) and Horizontal (pp) polarizations .....	53
27      Missile 5 ( <b>Test</b> ): Total RCS. Vertical (tt) and Horizontal (pp) polarizations .....	53
28      Missile 1 ( <b>Sim</b> ): RCS cut at 5 GHz. Vertical (tt) and Horizontal (pp) polarizations .....	54
29      Missile 2 ( <b>Sim</b> ): RCS cut at 5 GHz. Vertical (tt) and Horizontal (pp) polarizations .....	55
30      Missile 3 ( <b>Sim</b> ): RCS cut at 5 GHz. Vertical (tt) and Horizontal (pp) polarizations .....	55
31      Missile 4 ( <b>Sim</b> ): RCS cut at 5 GHz. Vertical (tt) and Horizontal (pp) polarizations .....	56
32      Missile 5 ( <b>Sim</b> ): RCS cut at 5 GHz. Vertical (tt) and Horizontal (pp) polarizations .....	56
33      Missile 1 Correlations (Sim/Meas) .....	57
34      Missile 1 Correlations (Sim/Meas) .....	58
35      Missile 1 Correlations (Sim/Meas) .....	59
36      Missile 1 Correlations (Sim/Meas) .....	60
37      Missile 1 Correlations (Sim/Sim) .....	61

Figure		Page
38	Missile 1 Correlations (Sim/Sim) .....	62
39	Missile 1 Correlations (Sim/Sim) .....	63
40	Missile 1 Correlations (Sim/Sim) .....	64
41	Missile 1 Correlations (Sim/Sim) .....	65
42	Missile 1 Correlations (Sim/Sim) .....	66
43	VGG-19, -10 dBm Confusion Matrix .....	67
44	VGG-19, -5 dBm Confusion Matrix .....	68
45	VGG-19, 0 dBm Confusion Matrix .....	69
46	VGG-19, 5 dBm Confusion Matrix .....	70
47	VGG-19, 10 dBm Confusion Matrix .....	71
48	Angle accuracy and Classification for the VGG-19 siamese network, SNR=-10 dB .....	71
49	Angle accuracy and Classification for the VGG-19 siamese network, SNR=-8 dB .....	72
50	Angle accuracy and Classification for the VGG-19 siamese network, SNR=-6 dB .....	72
51	Angle accuracy and Classification for the VGG-19 siamese network, SNR=-4 dB .....	72
52	Angle accuracy and Classification for the VGG-19 siamese network, SNR=-2 dB .....	73
53	Angle accuracy and Classification for the VGG-19 siamese network, SNR=0 dB .....	73
54	Angle accuracy and Classification for the VGG-19 siamese network, SNR=3 dB .....	73
55	Angle accuracy and Classification for the VGG-19 siamese network, SNR=5 dB .....	74
56	Angle accuracy and Classification for the VGG-19 siamese network, SNR=7 dB .....	74

Figure	Page
57 Angle accuracy and Classification for the VGG-19 siamese network, SNR=9 dB .....	74
58 Angle accuracy and Classification for the VGG-19 siamese network, SNR=11 dB .....	75
59 Angle accuracy and Classification for the VGG-19 siamese network, SNR=13 dB .....	75
60 Angle accuracy and Classification for the VGG-19 siamese network, SNR=15 dB .....	75
61 Angle accuracy and Classification for the VGG-19 siamese network, SNR=18 dB .....	76
62 Angle accuracy and Classification for the VGG-19 siamese network, SNR=20 dB .....	76

## List of Tables

Table	Page
1 VGG topology .....	21
2 Measurement parameters.....	28
3 Hyperparameter test factors.....	37
4 Model dimensions.....	45
5 VGG-16 test card listing teh evaluted configurations of the network. ....	78

Classifying Open-Air Target Measurements via Simulation Trained Convolutional  
Neural Networks

## I. Introduction

### 1.1 Problem Background

The Department of Defense Electromagnetic Spectrum Superiority Strategy states clearly that the Electromagnetic spectrum is a battleground, inseparable from the classical settings of war. The expectation for future near-peer conflict will result in a highly ‘congested, contested, and constrained Electromagnetic Operating Environment (EMOE) [1]’ The DoD EMSSS seeks to develop equipment that will be flexible, efficient, resilient. This project seeks to support this vision for the future EMS war by examining a potential means of reducing confusion and congestion in the EMOE.

Decoy airborne platforms were conceptualized as early as 1952 with the development and test of the XSM-73 ‘Goose’. The Goose was a ground-launched airborne decoy which was later reconfigured as an air-launched platform and re-designated the ADM-20 ‘Quail’. The Quail’s purpose was to be launched en-masse from an airborne platform in order to overwhelm an adversary Integrated Air Defense (IADS). With the enemy IADS occupied, bomber and strike aircraft would be able to penetrate the airspace and prosecute targets. Never employed in combat, the Quail retired and replaced by the ADM-141 Tactical Air Launch Decoy (TALD). The TALD was employed with good effect during the first night of the Gulf War. Launched in coordination with BQM-74 target drones, the TALD decoys were used to degrade the local IADs protecting Baghdad. The IAD operators were forced to turn on their tracking

and fire control radars, which were then targeted by allied anti radiation missiles. With the IADs systems destroyed or otherwise occupied, high priority targets were engaged by air to surface, and tomahawk cruise missiles. The operation was a success: adversary radars were forced to engage the unknown targets, which opened them up to attack from Coalition Anti-Radiation missiles [2]. The TALD provided an additional benefit: the attrition on the Iraqi Air Defense’s Surface to Air missile stores. The cheaply produced decoys were an effective sponge for the more costly surface to air missiles. The success of the TALD has motivated the development of the ADM-160b/C/C-1 Miniature Air Launch Decoy/Jammer (MALD/J). No longer restrained to a decoy role, these modern platforms are also capable of jamming victim radars.

Airborne decoys play a specific role in the contested EMOE: they degrade the air defenders view of the scene; force radars to engage the decoys, exposing themselves to anti-radiation fires; and force engagement, which depletes the IADS available surface to air missile stores. The power of decoy missiles is that on physical inspection they appear similar in shape size, and speed to their lethal relatives. An example is shown in figure 1, where an air-launched decoy is set alongside its potentially nuclear-equipped cousin.

This paper seeks a solution to this problem: a hypothetical sensor with an embedded machine learning model is trained to classify similar targets using radar cross section data. This project accepts the likelihood that the true RCS data for an adversary target would not be available, and instead utilizes simulation data to train the model. The models performance is tested using measurement data taken from an open-air range.



Figure 1: An ADM-160B MALD and AGM-86 Air Launched Cruise Missile (ALCM)

## 1.2 Research Objectives

The principle goals of this project are to analyze and document the performance of a machine learning network's ability to classify targets given radar cross section phasor data. The model will be trained using simulation data, and evaluated using measured data. Additionally, this paper will document data normalization techniques for RCS data; quantify classifier performance in terms of signal correlation; as well as document performance enhancing techniques such as multi-model comparators, and multi-angle training.

## 1.3 Document Overview

Chapter 2 of this document cover background information relevant to this project: radar operation, electromagnetic waves and target interaction, as well as a review of similar projects and the current state of machine learning models in signal processing. Chapter 3 will outline the methodology employed in this experiment to include data collection for both simulated and measured targets; measurement calibration; data augmentation, and model evaluation. Chapter 4 will report the experiments findings, and chapter 5 will present a conclusion measuring

## II. Background and Literature Review

### 2.1 Overview

An overview of the this project is presented in figure 2. Radar Cross Section (RCS) is collected from open air measurement, and simulation. Collected data is modified using Additive White Gaussian Noise (AWGN) to create both training and test datasets. Datasets are augmented, and passed to a machine learning model that will classify the targets as one of five potential targets. Training data will be used to determine optimal model parameters, and test data will be used to quantify accuracy. This conception: simulation data for training, measured data for evaluation is referred to as a ‘model based approach’. The primary performance measurements will be a confusion matrix, as well as a correlation matrix. The confusion matrix documents the models predictions, and whether they are correct or incorrect. The cross correlation matrix documents the ‘similarity’ between the targets RCS measurements, and will be the primary tool for understanding success or failure in classification accuracy.

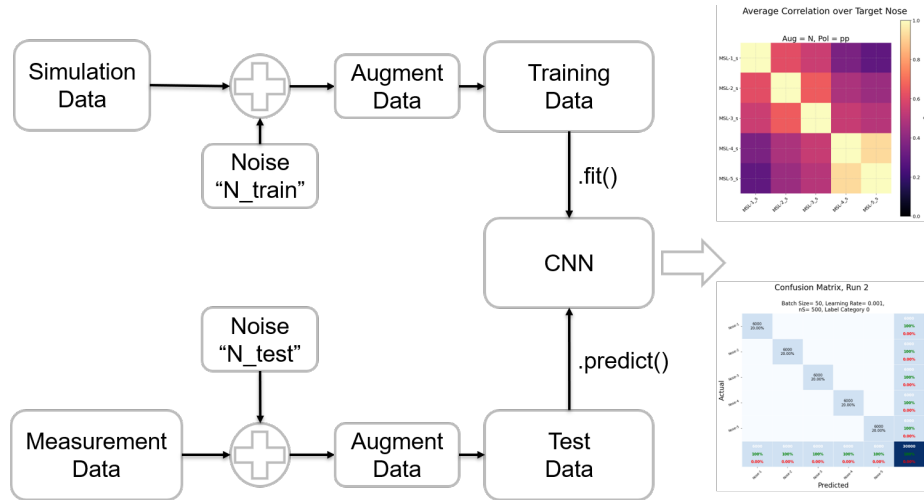


Figure 2: Project overview flow chart.

## 2.2 Simulation and Measurement Data

The simulation and measurement data used for project is captured/simulated using the reaction of metallic targets in the presence of electromagnetic fields. These fields are typically launched from a radar system, whose high transmission power and sensitive receiver allow the system to identify potential targets at long range. A radars theoretical performance can be quantified using the radar range equation, which incorporates the radars transmission power, sensitivity, as well as the target radar cross section. The omnipresence of noise degrades a radar's ability to detect targets. The radar's Signal to Noise Ratio (SNR) performance is a figure of merit that documents a radars capabilities in the presence of natural, or adversarial noise. The following sections will detail the phenomena listed above, as well as document how they will be employed throughout this project.

### 2.2.1 Electromagnetic Wave Interaction

Electromagnetic Radiation (EMR) as used by wireless systems is produced by the time-varying motion of charge. The mathematical model for EMR arises from solutions to Ampere's law with Maxwell's addition

$$\nabla \times \vec{B} = \frac{\partial}{\partial t} \mu \epsilon \vec{E} + \mu \vec{J}. \quad (1)$$

Here,  $\vec{B}$  and  $\vec{E}$  are the magnetic flux density and Electric Field strength respectively. The term  $\vec{J}$  represent source current, and is equal to zero in free space. The *intrinsic properties*  $\mu$  and  $\epsilon$  represent the magnetic permeability and electrical permeance of the material the fields are interacting with. These are the *constitutive relations* that link the interaction of a field with the physical world [3].

Ampere's law is a second order differential equation. When source current is equal to zero, it can be rearranged to take the form of the Helmholtz wave equation:

$$\nabla^2 \vec{E} - \mu\epsilon \vec{E} = 0. \quad (2)$$

Solutions to the Helmholtz wave equation that satisfy Maxwell's laws are Electromagnetic (EM) [3]. Assuming an EM wave polarized in the  $\hat{x}$  axis and propagating in the  $z$  direction, a solution would take the form:

$$\begin{aligned} \nabla^2 \vec{E} &= \mu\epsilon \vec{E} \\ \vec{E} &= \hat{x} E_0 \cdot \cos(kz - \omega t). \end{aligned} \quad (3)$$

The term  $k$  is the dispersion relation  $\omega\sqrt{\mu_0\epsilon_0}$ , and  $\omega$  is the frequency of oscillation for the time-varying signal displacement current.

The solution provided by equation 3 is useful for analyzing a waves interaction with material in free space. This wave will interact with any material whose intrinsic properties differ from the wave's dispersion relation. These regions are called *boundaries*, and demarcate a change in the intrinsic properties of the medium as seen by the wave. This paper will focus on the interaction of a wave in air as it meets a Perfect Electrical Conductor (PEC). A PEC is any material whose intrinsic properties make it appear to be a perfect conductor. The energy of the propagating wave, incident on a PEC wave will be completely converted to a surface current. This surface current produces a reflection of the incident wave [3]. The reflection produced by the boundary in the presence of incident EMR is what allows radars to operate. Assuming the reflections are sufficiently powerful, a detector can capture them and infer information

about the target.

### 2.2.2 Radar

The first Radio Detection and Ranging (RADAR) device was patented by German inventor Christian Hülsmeyer. Serving as a means to help ships avoid collision in heavy fog, radar showed impressive all weather long distance performance. This initial concept was expanded on by a British meteorologist named Robert Watson-Watt. Watt measured the EMR from lightning bursts using an oscilloscope as a means to track storms. Watt's innovation was using an oscilloscope to display the signals, which improved received signal fidelity compared to the Hülsmeyer detector. The British Air Ministry, sensing an impending war with Germany quickly pressed to militarize Watt's invention. In November 1934 the Committee for the Scientific Survey of Air Defense convened. Watt and his assistant Arnold 'Skip' Wilson proposed a radar system that could not only detect enemy aircraft, but could determine their range as well. The first operational pulse radar detected a Supermarine Scapa flying boat at a distance of 17 miles on 17 June 1935, ushering in the era of air defense radars in modern warfare [4].

Radar performance is commonly quantified using the radar range equation (RRE). The RRE is an extension of the radiation field solution using a far-field approximation [3], given by

$$P_r = \frac{P_t}{4\pi R_{r,t}^2} G_t \cdot \frac{\sigma(\theta, \phi)}{4\pi R_{t,r}^2} \cdot \frac{G_r \lambda^2}{4\pi} \quad (4)$$

where  $(\frac{P_t}{4\pi R_{r,t}^2} G_t)$  represents the transmitted signal power density attenuated over distance  $R_{r,t}$  from the radar to the target;  $(\frac{\sigma}{4\pi R^2})$  represents target interaction, echo emission, and echo attenuation over distance  $R_{t,r}$ ; and  $(\frac{G_r \lambda^2}{4\pi})$  models receiver gain and sensitivity. [5].

The terms  $P_t$  and  $P_r$  represent the transmitted power of the initial signal, and the received echo signal respectively. The gain terms  $G_t$  and  $G_r$  represent the directionality of the transmit and receive antennas respectively, and are equivalent for a mono-static radar configuration. A mono-static radar utilizes a single antenna to both transmit and receive signals.

Target interaction leverages the behavior of electromagnetic waves at boundaries as discussed in section 2.2.1. A metallic, or PEC target will re-emit an echo signal with a directional intensity given by its RCS pattern,  $\sigma(\theta, \phi)$ . The response of  $\sigma$  is primarily driven by the physical shape of the target. A principle of low-observable design seeks to control  $\sigma$  by directing scattered pulses away from the mono-static radar.

The receiver term shows a dependence on frequency for  $\lambda = c/f$ , where  $c = 3 \times 10^8 [m/s]$ , and  $f$  is the carrier frequency of the transmitted signal. This frequency dependence is driven by antenna design. Antennas have an optimal shape that is tailored to their operating frequency band. The antennas used for this experiment are within their operating bands for all frequencies. However, this frequency dependence will play an important role in equipment calibration, which will be discussed in section 2.3.

### 2.3 Measurement Calibration

Open air measurements must account for two distinct error sources: range intrusion, and instrument calibration. Range intrusion accounts for spurious echo's from the floor, walls, target mount, and other physical objects in the range that interact with the incident field. These signals constitute the ‘background’ of the scene and can be mitigated in two ways: 1. gating returns at the receiver to create quiet zones; 2. Implementing background subtraction using

$$E_{t,true} = E_{t,raw} - E_{t,bg} \quad (5)$$

where  $E_{t,raw}$  and  $E_{t,bg}$  are measurements of the scene with and without the target in place. While background subtraction will help to reduce spurious signals, it cannot account for target-mount interactions and will not completely eliminate spurious returns.

The instrument radar is calibrated using the substitution method: a simple target whose RCS can be readily calculated is used to create a proportionality constant which accounts for deviations in radar performance [6]. Since the range distances are fixed, the only factor of the radar range equation that will change is either the target's RCS, or fluctuation in transmitted power over frequency. By measuring a target with a known RCS, the proportionality constant  $C$  can be determined using

$$C = \frac{E_{cal,sim}}{E_{cal,raw} - E_{cal,bg}} \quad (6)$$

where  $E_{cal,raw}$  and  $E_{cal,bg}$  are measurements of the scene with and without the calibration target respectively. The term  $E_{cal,sim}$  is the RCS measurement of the calibration target. This experiment utilizes a 7 inch calibration cylinder whose RCS is modeled using CADFeko. Notably, the substitution method employs background subtraction as discussed previously.

Prior to data processing, all target measurements are calibrated using

$$E_{t,true} = \frac{E_{t,raw} - E_{t,bg}}{E_{cal,raw} - E_{cal,bg}} \quad (7)$$

## 2.4 Instrumentation Quiet Zone

An instrumentation radar can be configured to exclude radar echoes that are outside of a desired location. This is desirable when collecting data. The receiver of the radar is *gated*, or configured in a manner to only ‘listen’ for echoes during a certain window. The windows are configured in temporal time. Due to the speed of light, these temporal time values directly correspond with a location using

$$d = \frac{c \times \Delta t}{2} \quad (8)$$

where  $d$  is a distance in meters,  $c$  is the speed of light in  $m/s$  and  $\Delta t$  is elapsed time. This equation is divided by 2 due to the two-way path a radar pulse must travel. As an example, a preferred quiet zone that begins 5 meters from the radar, and ends 10 meters from the target would have a reception time window between 33.3 and 66.7 nano seconds.

## 2.5 Signal to Noise Performance

A radars operational ‘field of view’ is limited by the sensitivity of its receiver. Field of view in this context refers to the distance and azimuth over which the radar can successfully identify and prosecute targets. Sensitivity measures the minimum signal level that the radar can detect. If a signal is too faint, it will fall below the noise floor of the system and become irrecoverable.

The noise floor defines the power level,  $P_n$  below which received signals will be lost. Typically, the noise floor is driven by the thermal noise of the radars receiver. Thermal noise current accounts for the random fluctuations of moving charges in matter above 0K and can functionally defined as

$$P_n = k_B T_S B = k_B T_0 F B \quad (9)$$

Where  $k_B$  is Boltzmann's constant <sup>1</sup>,  $T_S$  is the system temperature in Kelvin,  $B$  is the instantaneous receiver bandwidth in Hz,  $T_0$  is the standard temperature <sup>2</sup>, and  $F$  is the noise figure of the receiver subsystem. System bandwidth is typically driven by the signal the radar emits, and cannot be made arbitrarily small. A radar pulse of length  $\tau$  will require a bandwidth of  $B = 1/\tau$  [7][8][9]. A hypothetical system with a noise figure of  $F = 1.2$ , and bandwidth  $B = 1$  MHz will have a noise floor of  $-112.8$  [dB.m].

Thermal noise is modelled as an additive zero-mean gaussian process. Modern radar designs seek to mitigate thermal noise via pulse integration. Adding multiple pulses together reduces noise power since the zero-mean noise tends to zero over multiple integrations. For a coherent system (one in which phase is maintained) the improvement in signal level is directly proportional to  $n$ , the number of pulses integrated. For a non-coherent system, the integration factor is given as  $\sqrt{n}$ .

The radar equation can be re-cast to include thermal noise and the integration factor using

$$SNR_0 = \frac{P_t}{4\pi R_{r,t}^2} G_t \cdot \frac{\sigma(\theta, \phi)}{4\pi R_{r,t}^2} \cdot \frac{G_r \lambda^2}{4\pi} \cdot \frac{1}{k_B T_S B} \cdot n_p \quad (10)$$

where  $SNR_0$  represents the signal to noise ratio of the received signal with respect to the thermal noise in the system. The minimum discernable signal (MDS) of the system is the smallest SNR for which the radar can reliably detect targets in the presence of thermal noise.

This paper will take measure the SNR as the ratio of the absolute value of phasor

---

<sup>1</sup> $1.38 \times 10^{-23} W \cdot s/K$

<sup>2</sup> $T_0 = 290K$

RCS data and noise in milli-decibel (dBm). A milli-watt decibel is the measure of a signal in decibel form, referenced to 1 milli-watt:

$$dBm = 10 \times \log\left(\frac{P[W]}{0.001[W]}\right) \quad (11)$$

## 2.6 Radar Cross Section

RCS is the ratio of scattered to incident power for a given target in the presence of an EM wave. RCS data can be presented in several ways depending on the context, and what information is most relevant. In each of the following cases, data is collected and presented for both vertically and horizontally polarized incident fields. The figures in this section will present horizontally polarized data for expedience.

An RCS ‘cut’ is a polar plot of RCS data taken at a single measurement frequency over 360 degrees. Total RCS is presented as a contour plot with frequency and angle axes, and magnitude represented by color. The augmentation applied to the data plays an important role in data presentation, since RCS phasor data can have a large dynamic range. Large contributions can be highlighted or suppressed dependent on the augmentation employed. This project will use both plot formats, and several augmentation schemes throughout.

As an example of plot format, augmentation style, and the behavior of targets in incident field, consider the simulated RCS response of the target shown in figure 3. The total response, as well as an RCS cut augmented in  $m^2$  and  $db_{sm}$  are shown in figures 4, and 5 respectively.

The  $m^2$  format is calculated using the IEEE definition for RCS,

$$\sigma[m^2] = 4\pi \frac{|E_s|^2}{|E_i|^2} \quad (12)$$

where  $E_s$  and  $E_i$  are the scattered and incident fields, and  $r$  is the distance between

the transmitting source and target 12[6]. This data can be re-cast in  $\text{dB}_{sm}$ , or decibel per square meter as follows:

$$\sigma[\text{db}_{sm}] = 20 \times \log \left( \frac{\sigma[m^2]}{1[m^2]} \right) \quad (13)$$

The augmentation employed highlights the RCS contribution based on the targets physical construction. In figure 4 data is presented in  $m^2$  format. The specular flash of the cylindrical missile body dominates the return. In figure 5, the response of the cylindrical body is suppressed, and other RCS contributions can be observed. This project will restrict classification to a sector surrounding the targets nose. Extending  $\pm 30^\circ$  about the target nose, the sector of interest is shown as a green wedge on the RCS cuts. On the total RCS plots, measurements outside the 60 degree sector are ‘dimmed.’

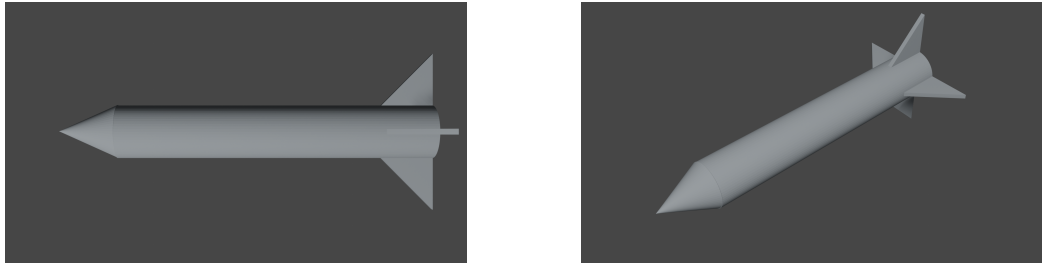


Figure 3: Top and side view of a missile target.

The RCS cut of the model is used to give a quick at-a-glance view of the targets RCS deviation over angle. While this is useful on inspection, it is less useful for this project. Ideally, the sensor under examination would be able to make a classification using the data from a single angles measurement. This data would correspond to a single column of data taken from a total RCS contour plot. This single column contains 101 frequency measurements, ranging from 4.5 - 5.5 GHz. An example of frequency deviation for a single angle is shown in ???. This project focuses heavily on this frequency deviation. Conceptually, the construction of each target should diverge

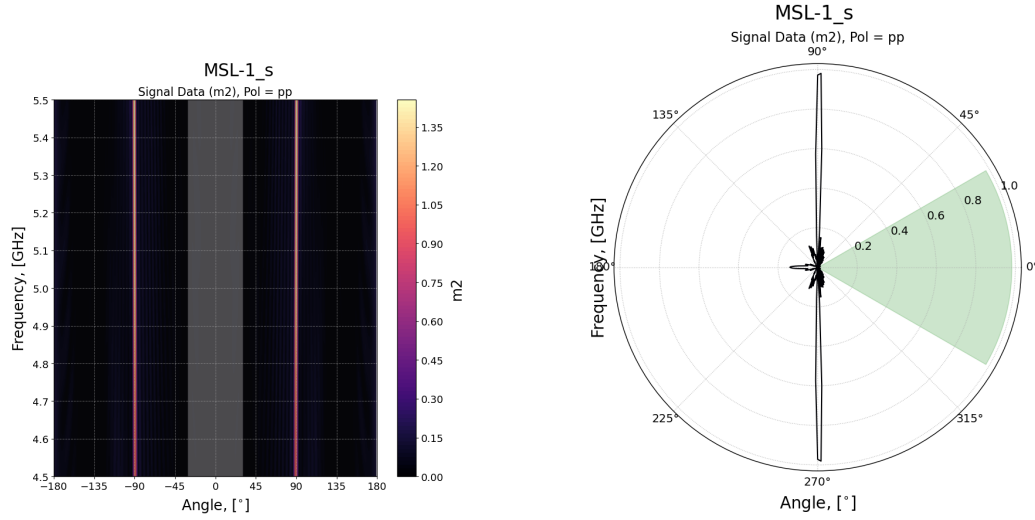


Figure 4: An RCS measurement at 5 GHz over all angles, and the total RCS measurement of a missile target in  $m^2$ .

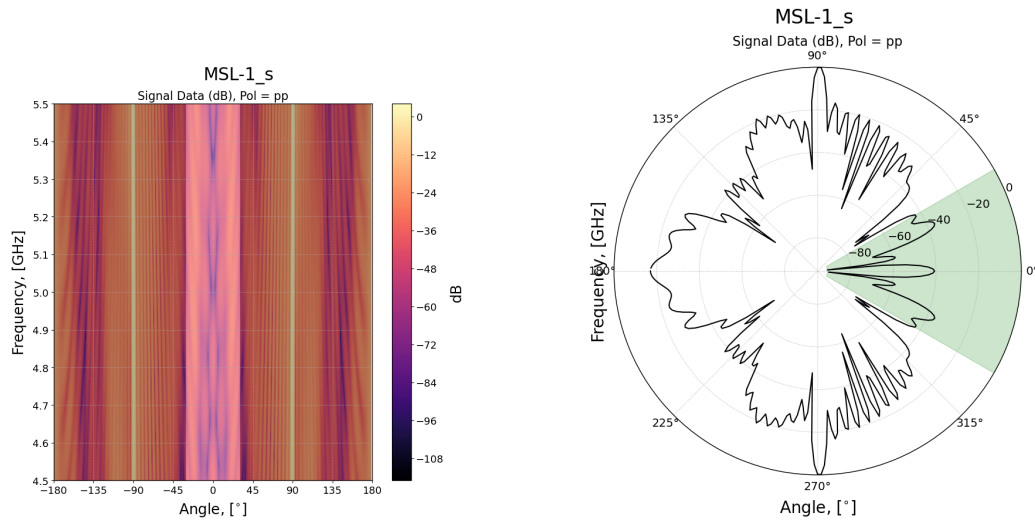


Figure 5: An RCS measurement at 5 GHz over all angles, and the total RCS measurement of a missile target in  $\text{dB}_{sm}$ .

enough to produce unique RCS responses.

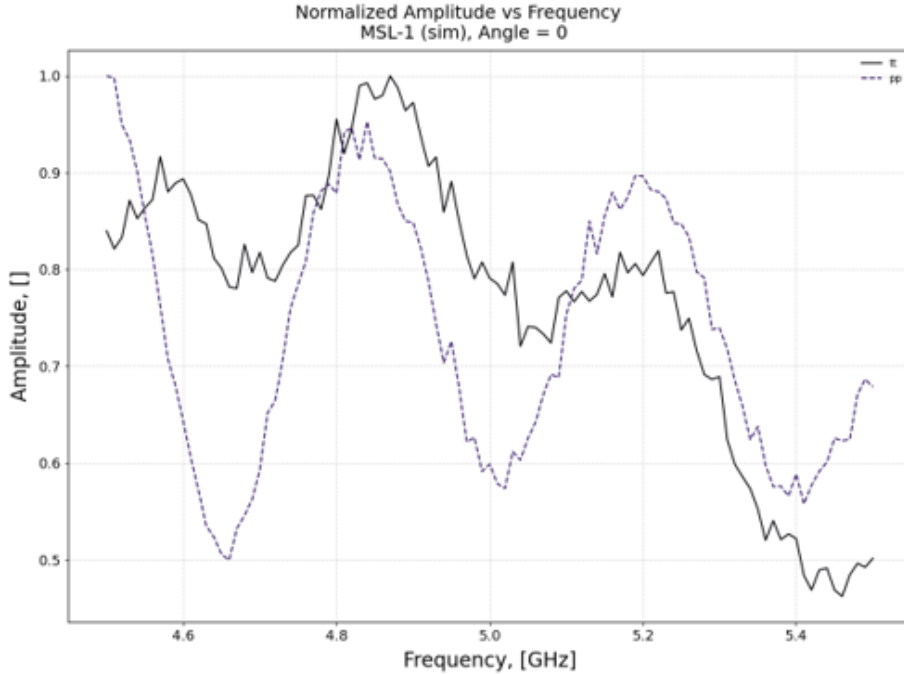


Figure 6: Frequency deviation over a single angle.

## 2.7 Machine Learning Models

Advances in computer power, and the development of readily available software has made machine learning a common and powerful engineering tool. A machine learning model is an algorithm that is *trained* rather than programmed. Training is the process of passing examples of a task or behavior to the model, and allowing it to adjust its *parameters* to reach a desired outcome. The examples used to train a model include: input data points or *features*; and *labels*, the expected outcomes for each set of features [10].

The application of machine learning models to radar signal classification has been thoroughly studied: Deep Learning models, Residual Neural Network (RNN), tree regressors, random forests, state-vector machines as well as neural and Convolutional

Neural Networks (CNN) have been documented to show promising performance [11]. The remote sensing community has also employed machine learning in target identification, which will be discussed in section 2.9.

Given the recent growth in CNN toolsets and previous success in classifying RCS frequency-series data this paper will focus on 1-Dimensional CNNs[12]. Originally developed to solve computer vision problems, CNNs are being employed with success in increasingly more problem sets to include radar signal classification, electrocardiogram analysis, structural failure modes, and remote sensing [13]. Two model topologies will be employed: VGG-19, and ResNET. The first, VGG-19, is a simple, sequential, and very deep model. The second, ResNET, is a non-sequential residual network that favors ‘lateral’ over vertical depth. Each topology will be discussed in detail in the following sections.

### 2.7.1 Deep Learning

Convolutional Neural Networks are a subset of *Deep Learning* models. ‘Deep’ in this sense refers to depth-of-model as opposed to something philosophical [10]. The original deep learning networks were conceived in 1943 [14] as artificial neural networks (ANNs). These networks borrowed from the construction of the human neuronal cortex to develop a simplified computation model based on a network of connected nodes. The nodes, or neurons of an artificial neural network are built to produce an output, for a given input. A perceptron, one of the simplest ANN architectures is shown in figure 7 as an example [15].

The inputs  $x_1, x_2, \dots, x_n$  are *weighted* by  $w_1, w_2, \dots, w_n$ , summed using

$$z = w_1x_1 + w_2x_2 + \dots + w_nx_n = x^T w \quad (14)$$

and passed to the perceptron. If the weighted sum  $z$  is larger than some threshold,

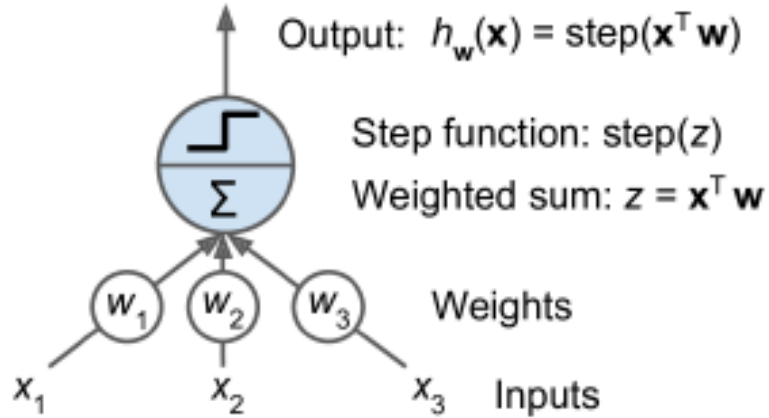


Figure 7: Perceptron model taken from ‘Hands on Machine Learning’[15].

it will trigger the node’s *activation function*. An activation function is a response function that produces an output for a given input. Here, the activation function is a Heaviside step given as

$$h_w(x) = \text{step}(x^T w). \quad (15)$$

This activation function will step from zero to one if its threshold is reached. Alternate activation functions are detailed in the appendix. Deep learning models stack these weighted nodes into a ‘Dense’ layer, and connected with other dense layers. The resulting series of connections and weights form the deep learning model’s *topology*.

The weights for each node in the model are found using the following algorithm [10]:

1. Feed a batch of training samples to the model.
2. Run the network for each sample  $x$ , and record the models prediction  $y_{pred}$
3. Compute the loss between samples label  $y$  and  $y_{pred}$
4. Compute gradient of the loss with regard to the network’s parameters

5. Update the weights of the network in a way that slightly reduces the loss for the samples in the next batch

Steps 1 and 2 take input data as a *batch*, or a collection of multiple input samples has the model process them and make a prediction. The ‘distance’ between the sample’s label  $y$  and the model prediction  $y_{pred}$  is measured using a *loss function*. Steps 1 and 2 are called the *forward pass*. The process of updating the weights is done using *stochastic gradient descent, (SGD)* and the *back propagation* algorithm [16]. When utilizing the TensorFlow package, all inputs, and model objects are tensors and can be manipulated using tensor operations. The SGD algorithm takes the tensor gradient of the model’s loss function to determine a minima in step 4. Step 5 in the algorithm moves the weights away from this minima [10]. Ideally, adjustments in the models parameters will reduce the loss function for the next batch of inputs.

The concept of layers, weights, and the training algorithm are directly applicable to convolutional neural networks. The change from ANNs to CNNs is the structure of each ‘node’ and the overall topology of the network.

### 2.7.2 Convolutional Neural Networks

Early neural networks were built using dense layers of nodes. The nodes of each layer connected to the nodes of other layers and interacted with varying levels of strength determined by their weights. These networks develop pattern recognition *globally*. The entire input is considered when producing an output. Convolutional neural networks work to identify *local* patterns [10]. This is done by using the process shown in figure 8.

An 8x8 array of input data is passed to the model (orange). A padding (light orange) is applied to the perimeter, and the data is sampled by a convolution window (dotted red, 3x3). The convolution window performs a convolution operation on all

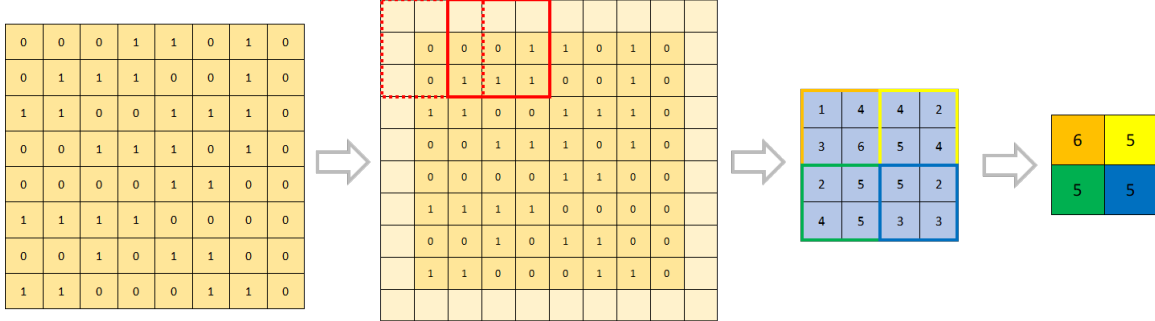


Figure 8: Convolution process: Input Data - $\downarrow$  Convolution - $\downarrow$  Max Average.

data elements that fit inside it, before moving to the next batch of values (solid red, 3x3). The output of the convolution operation (which employs the layer’s weights) is the *kernal*, and is used to reassemble the data post convolution (light blue). The convolution window is then shifted by a distance determined by the layers *stride*. In this case, the stride of the layer is 2. The convolution process is repeated until the entire input space has been sampled. The resulting output (blue) is then down-sampled using a pooling process. In this case, a pooling window of size 2x2, and stride 2 pulls the maximum value in its view. This is referred to as max pooling. Alternate pooling schemes such as average, and min pooling can also be employed.

### 2.7.2.1 VGG-19

Developed at the University of Oxford, the VGG topology was designed to increase accuracy for image recognition tasks. Utilizing a small receptive field, simple construction, and multiple stacks of convolution layers for each pooling operation, the VGG topology exceeded the performance of earlier CNN models [17]. The key feature of the VGG topology is vertical depth. The developers found the increase in model depth was directly correlated with performance, particularly with complex inputs.

This project utilizes the VGG-19 topology listed in table 1. The convolution layers

share a 1x3 receptive field, with a stride of 1 and ‘ReLU’ activation functions. The max-pooling layers are 2x2 with a stride of 2. The convolutional layers terminate with a ‘flattening’ layer. This layer prepares the convolutional data to be passed to a dense network. The neural network features ‘dropout’ layers. Drop out layers exclude samples within a batch, and help to prevent overfitting in the model. The final layer utilizes a ‘softmax’ activation function. This activation calculates a probability for each label in the training data, and produces a prediction.

#### 2.7.2.2 ResNET

**Batch Normalization:** Maintains a mean output close to zero, and the output standard deviation close to 1 [18].

**Dropout:** randomly sets input units to 0 with a frequency set by the *dropout rate*. This helps to prevent overfitting during model training [18].

Layer	Name	Input Shape	Output Shape
0	Input	[101, 2]	[101, 2]
1	1D-Conv(64)	[101, 2]	[101, 64]
2	1D-Conv(64)	[101, 64]	[101, 64]
3	1D-MaxPooling	[101, 64]	[50, 64]
4	1D-Conv(128)	[50, 64]	[50, 128]
5	1D-Conv(128)	[50, 128]	[50, 128]
6	1D-MaxPooling	[50, 128]	[25, 128]
7	1D-Conv(256)	[25, 128]	[25, 256]
8	1D-Conv(256)	[25, 256]	[25, 256]
9	1D-Conv(256)	[25, 256]	[25, 256]
10	1D-Conv(256)	[25, 256]	[25, 256]
11	1D-MaxPooling	[25, 256]	[12, 256]
12	1D-Conv(512)	[12, 256]	[12, 512]
13	1D-Conv(512)	[12, 512]	[12, 512]
14	1D-Conv(512)	[12, 512]	[12, 512]
15	1D-Conv(512)	[12, 512]	[12, 512]
16	1D-MaxPooling	[12, 256]	[6, 256]
17	1D-Conv(512)	[6, 256]	[6, 512]
18	1D-Conv(512)	[6, 512]	[6, 512]
19	1D-Conv(512)	[6, 512]	[6, 512]
20	1D-Conv(512)	[6, 512]	[6, 512]
21	1D-MaxPooling	[6, 512]	[3, 512]
22	1D-Flatten	[3, 512]	[1, 1536]
23	Dense(4096)	[1, 1536]	[1, 4096]
24	Dropout(50%)	[1, 4096]	[1, 4096]
25	Dense(4096)	[1, 4096]	[1, 4096]
26	Dropout(50%)	[1, 4096]	[1, 4096]
27	Dense(1000)	[1, 4096]	[1, 1000]
28	Softmax(5)	[1, 1000]	[1, 5]

Table 1: Model dimensions

## 2.8 Optimizers and Augmentation

Deep learning network optimizers utilize Neural network optimizers work best when the input data is augmented [12]. The augmentation processes used for this project are documented in section 3.5.2.

## 2.9 Training

Target recognition is the process of a sensor categorizing a target in its field of view given some training, or a pre-planned procedure. The remote sensing community has been experimenting with machine learning applications and their potential to increase classification accuracy for automatic target recognition with synthetic aperture radars. These ML models are pre-trained, and embedded within the radar receiver. A 2016 study documents three training regimes that have been employed to develop successful ML models: 1. Feature based training; 2. Semi-model based training; 3. Model based training [19].

The similarity in operation of a SAR and traditional radar make these training regimes applicable to target identification in air defense radars. A strictly feature based approach would utilize an incomplete set of RCS measurements to train a sensor; a semi-model based approach would leverage the characteristics of a feature based test-set to create a more robust training set; and a model-based approach would attempt to create a full set of training data using model and simulation.

This experiment will utilize a model-based training approach. The simulated RCS response of XX targets will be used to train a machine learning algorithm, and the accuracy of the model will be tested using measurement data.

### **2.9.1 Feature-Based Training**

The most common approach, feature based training utilizes either raw or template image-data to train a sensor. Template data is typically a snap-shot of a target in a specific ‘pose’. Pose in this context refers to the targets configuration with respect to the sensors viewing angle. Features include target size, configuration, as well as the statistical properties of the received signal. While deeply researched and computationally accessible, feature based training suffers from statistical classification breakdown and pattern recognition problems [19]. Governments and their militaries go to great lengths to set a standard for how national secrets are classified and controlled [20][21], restricting the amount of reliable template data available for training.

Borrowing this concept for training a traditional radar: assume a template image to be the echo response from a target at a single aspect-angle. This template will contain useful features for training a machine learning model. However, if the amount of templates for a target are limited, the model could over-train to the incomplete information and miss-classify unfamiliar pose angles.

### **2.9.2 Semi-Model Based Training**

Semi-model based training extends the concept of feature based training, while attempting to build a more complete training set given limited template data.

Semi-model training data seeks to extract characteristic data from the training templates: scattering center locations, counts, and intensities are used to generalize the expected response from the target. from both feature and model based training: the limited feature based data set is processed to produce scattering center models. This method seeks the best of both world: robust, ‘behavior’ based models that are built with limited, but readily available data sets.

### **2.9.3 Model-Based Training**

Model based training utilizes ESIM software to produce training data. In its simplest conception, the ‘model based’ approach can be thought of as a data generator for a feature based training regime. That is, a system can be trained to identify features using modeled data, providing a sensor with otherwise inaccessible data.

Alternately, generated models can be processed to provide the sensor with a more ‘bottom-up’ training approach. The ‘bottom-up’ concept was developed and implemented by Robert A. Brooks at MIT for the ACRONYM target recognition system [22][23]. This method shifts the focus of training away from what the target looks like in a specific, limited instance and focuses on the more general representation of *how* the target *may* look.

### III. Methodology

#### 3.1 Overview

Initial experiments are completed to determine the optimal hyperparameters for the neural network. Networks are trained using multiple level of training noise to test for ideal performance. The optimal models will then be placed in a ‘Siamese network’ – a configuration that takes the classification values from multiple models and determines the ‘best fit’ classification for the given input data.

#### 3.2 Targets

Five target models were chosen for this experiment. Each model is a missile-surrogate with a shared fuselage, and a unique nose cone. The dimensions of the fuselage and the nose cones are listed in table 4. Nose cones 1-3 are simple cones with a fixed base diameter and edge length. Nose cones 4 and 5 are curved. They share the common 3 inch base diameter, with differing diameters as they extend from the base to tip. The additional measurements represent the diameter of the cone at equally spaced intervals along the edge from base to tip. Each model is made of aluminum as is assumed to behave as a PEC in the presence of EMR. The Cad models of each missile nose is shown in figures ??, ??, and ???. The side and top view of the missile is shown in figure 9.

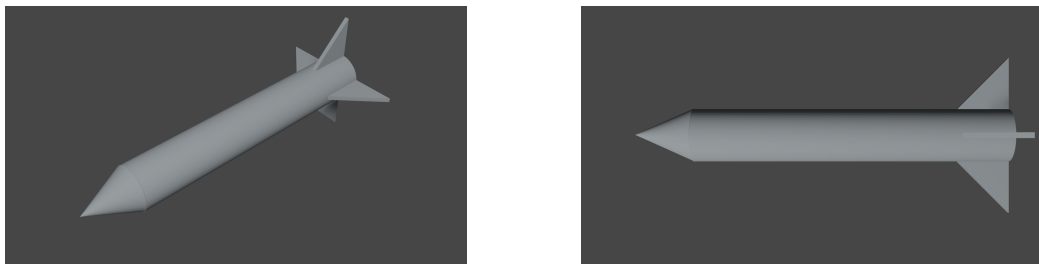


Figure 9: Side and top view of the missile surrogate (Cad model)

Simulation models were developed using Blender 3d, and exported as .stl mesh models. Mesh models were converted to solids from mesh, and exported as .step geometries using FreeCad. The .step format worked well with CADFeko’s internal meshing system. Since Blender 3D does not export .step natively, the additional step of importing the .stl mesh into FreeCad was necessary.

### 3.3 Measurement

The targets were measured at the Air Force Institute of Technologies (AFIT) Compact Radar Range. The layout of the AFIT range is shown in figure 10. The range uses a BlueMax G6 instrumentation radar (blue items in schematic), with a Vivaldi wide-band antenna configured in both horizontal and vertical polarizations. Transmitted signals are directed at a curved reflector located 3 meters from the antenna. Ideally, the incident field will be a plane wave. That is, the wave front is the same when measured vertically or horizontally. However, the short distance between the antenna and the target will produce a curved wave-front surface. The reflector helps to ‘flatten’ the wave front, and make it appear more planar.

Targets are placed on a foam column located 7 meters from the reflector. The column is 2 meters tall, and can rotate 360 degrees. Foam is used, as its intrinsic properties are similar to air, and do not contribute significantly to scene clutter.

The radar can capture measurements over multiple frequencies, polarizations, and target aspect-angles. Measurements are returned as complex voltages  $M$ . A measurement is collected using a specific carrier frequency  $f$ , at a single aspect angle  $a$ . For example, measurement  $M_0$  is collected by launching a stream of pulses with carrier frequency  $f_0$  at a target presenting a fixed aspect angle  $a_0$ . The receiver will collect and integrate  $N$  echo pulses and store the value as  $M(f_0, a_0)$ . This process is repeated over the desired range of frequencies and angles resulting in a matrix

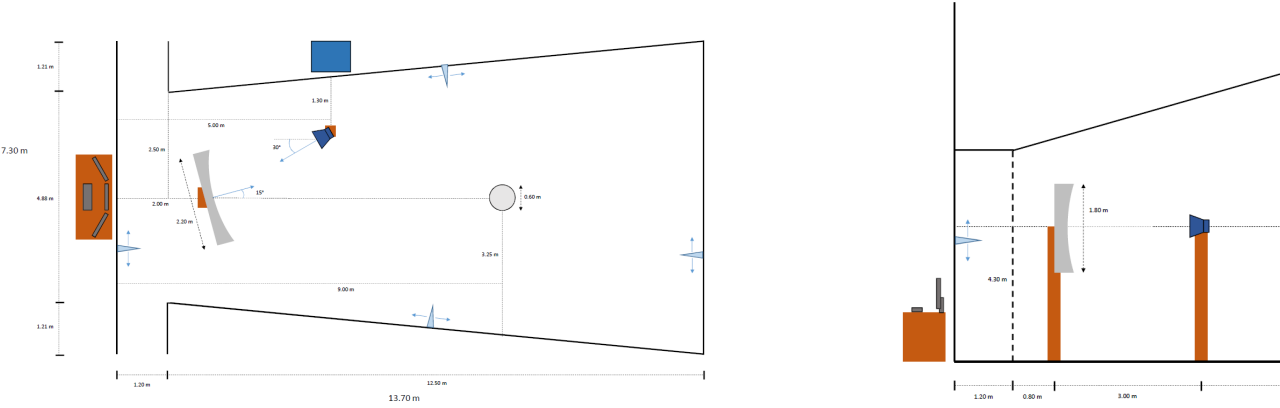


Figure 10: Top-down and side view of the AFIT compact radar range.

$$E_{tt} = \begin{bmatrix} M_{0,0} & M_{0,1} & \cdots & M_{0,A} \\ M_{1,0} & M_{1,1} & \cdots & M_{1,A} \\ \vdots & \vdots & \ddots & \vdots \\ M_{F,0} & M_{F,1} & \cdots & M_{F,A} \end{bmatrix} E_{pp} = \begin{bmatrix} M_{0,0} & M_{0,1} & \cdots & M_{0,A} \\ M_{1,0} & M_{1,1} & \cdots & M_{1,A} \\ \vdots & \vdots & \ddots & \vdots \\ M_{F,0} & M_{F,1} & \cdots & M_{F,A} \end{bmatrix} \quad (16)$$

where  $E_{tt}$  and  $E_{pp}$  represent measurements taken for the vertical and horizontally aligned incident wave polarization. Each row in the matrices corresponds to 360 aspect angles measured at one frequency. The total array shape is  $F \times A$ , where  $F$  and  $A$  are the number of frequencies and angles captured respectively.

Table 2 lists the measurement parameters used for this experiment.

The radar used for this project produces a discrete RCS measurement at individual frequencies as opposed to a time domain response for each pulse. Since this time-domain information was unavailable, this experiment attempts to recreate the time-domain response, by capturing discrete measurements for each frequency and stitching them together into a frequency domain equivalent for the expected time-domain response.

The integration factor was chosen to provide sufficiently accurate measurements. This ideal measurement serves as a signal to noise performance baseline. The receiver

Transmitter Power:	40[dBm]
Tx Gain: 15[dB]	
Rx Gain: 15[dB]	
IF BW: 200[kHz]	
Noise Figure, $F$ : 3[dB]	
Tx Loss: 4.5[dB]	
Rx Loss: 4.5[dB]	
Operating Temp: 68[F]	
Pulse Width:	10[ns]
Frequency Range:	4.5 – 5.5[GHz], 10[MHz] step
Aspect-angle Range:	0 – 360°, 1° step
Integration Factor:	1024
Transmit Delay :	330 [ns]
Receiver Delay :	434 – 446 [ns]

Table 2: Measurement parameters.

delay of 434 – 446 [ns] puts the quiet zone window at approximately 76 meters when accounting for the reducing transmission speed of waves in transmission line. The target fixture is located 14 meters from the antenna, with the remaining distance accounted for by feedline from the instrument to the antenna. This window was confirmed by ‘walking’ the range. This operation transmits pulses from the antenna, and shifts the reception window until a known target is captured in the desired quiet zone.

### 3.4 Simulation

Simulations were completed using Altair’s CADFeko Electromagnetic Simulation Suite. CADFeko uses an iterative Method of Moments - Separation of Principles (MOM-SEP) algorithm to compute the RCS response of the target model. The output data from the simulation is in phasor form. Method of Moments is used to calculate scattering for targets in the resonant regime: when physical target size is roughly the same size as the incident wave length, but less than 10 times larger [6]. At 5 GHz, the incident wave length is 60 millimeters. At 457mm, the fuselage body

is 7.62 times larger than the 5 GHz wavelength placing towards the upper end of the resonant regime. The nose cones range in size from 101 to 228 mm, which fit comfortably in the resonant regime.

### 3.5 Data Processing

#### 3.5.1 Data Set Generation

In order to mimic the expected response of a radar pulse, training and test data sets are built by slicing the RCS matrices shown in equation 16 column wise. The resulting vectors

$$F_{tt}(f, a_n) = \begin{bmatrix} M_{0,a_n} & M_{1,a_n} & \cdots & M_{F,a_n} \end{bmatrix}, F_{pp}(f, a_n) = \begin{bmatrix} M_{0,a_n} & M_{1,a_n} & \cdots & M_{F,a_n} \end{bmatrix} \quad (17)$$

contain the measurements  $M(f, a_n)$  for all frequencies  $f$ , at a specified angle  $a_n$  for the vertical and horizontal polarizations respectively. Each vector corresponds to the frequency content of an integrated pulse stream for each pose angle of the target. The training data set can be made arbitrarily large by multiplying frequency slices and applying random additive noise with power  $N_{train}$  to create variance in each sample.

Each sample in the training data set is assigned a label that corresponds to the ‘sector’ that each sample falls in. Sectors are chosen such that RCS characteristics specific to the target fall in the same sector. This experiment utilizes either 3 or 4 90-degree sectors centered on the nose, tail, and sides of the target. The three label case collapses the sides of the fuselage into a single label.

Test data sets are built similarly: frequency vectors are extracted from the measurement array, and additive noise with power level  $N_{test}$  is applied.

### 3.5.2 Data Augmentation

During training, neural networks optimize their decision weights by utilizing an ‘optimizer’. An optimizer is a method of testing whether the network is adjusting its weights in a way that maximizes its ability to categorize the input data correctly. This experiment utilizes a Stochastic Gradient Descent optimizer (SGD). This method favors adjustments in the networks weights that push towards a minimization of error in categorization. Since this is a method that utilizes slopes, differentiation is employed. In order to prevent unnecessarily large slopes, data is augmented. There are two forms of data augmentation that are typically employed: standardization, and normalization.

Standardization takes the maximum value in the current training array, and scales the entire array. This creates a data range between 0 and 1. Standardization of data in this experiment is done using

$$F_{tt}(f, a_n) = \left[ M_{0,a_n} \quad M_{1,a_n} \quad \dots \quad M_{F,a_n} \right] / \max(F_{tt}(f, a_n)) \quad (18)$$

where the function `max()` pulls the max value in the vector.

Normalization extracts the mean and standard deviation of the vector and returns a ‘Z-Score’ for each cell in the array using

$$F_{tt}(f, a_n) = \frac{\left( \left[ M_{0,a_n} \quad M_{1,a_n} \quad \dots \quad M_{F,a_n} \right] - \mu \right)}{\sigma} \quad (19)$$

where  $\mu$  is the mean value of the vector, and  $\sigma$  is the standard deviation.

### 3.5.3 Comparison

Signals are compared using a cross-correlation function. The cross correlation function measures the similarity between two signals, and outputs a correlation co-

efficient,  $\rho$ . Values for  $\rho$  range from  $\pm 1$  for correlated, and anti-correlated signals respectively, and 0 for un-correlated signals. As an example, the cross correlation of a signal with itself, will have  $\rho = 1$ .

Signal similarity is measured over all frequencies, at each angle using

$$\rho = \text{Corr}(E_{1,tt/pp}(f, a_i), E_{2,tt/pp}(f, a_i)) \quad (20)$$

where  $E_{1,pol}$  and  $E_{2,pol}$  RCS phasor response measurements for signals 1 and 2, at angle  $a_i$  and polarization  $pol$ , over all frequencies  $f$ . Signals will be selected from the pool of simulated and measured RCS response. Measuring the correlation strength of all targets with one another will serve as a means of identifying breakdowns in target classification. The correlation function is always applied to signals with similar polarizations.

To measure the breakdown in signal correlation as noise is applied, the following algorithm is employed:

1. Signals 1 and 2 are selected
2. Noise is applied to signal 1 and signal 2
3. Signals one and two are augmented per angle
4. Equation 20 is applied for each angle
5. The resulting vector of correlation coefficients is plotted against angle

Correlation performance is reported in SNR. The SNR for each target is the average phasor value of all data elements in the matrices  $E_{tt}$  and  $E_{pp}$  for each target.

### **3.6 Neural Network Development**

### **3.7 RCS Calculation**

## IV. Results and Analysis

### 4.1 Preamble

The simulation and measurement results are captured using the methods described in sections 2 and 3. A comparison between the simulation and measurement targets is completed by calculating the correlation of each targets frequency vector, at each angle. This correlation function results in a single correlation coefficient for each angle.

Generally, the correlation coefficient is below one (a perfect match between measurements). Missile 1 showed the highest correlation between its measurement and simulation, with a mean correlation coefficient of 0.862, and standard deviation of 0.092. The mean correlation of the succeeding targets decreased with each continuously, with missile 5 showing the lowest mean correlation of 0.082, and standard deviation of 0.234.

These breakdowns in correlation between measurement and simulation are expected to impact the capability of the classifier. A classifier will be considered a ‘failure’ if it cannot exceed an accuracy of 20%, equivalent to randomly guessing the targets label.

### 4.2 Measurment Results

Figures 18-22 represent the calibrated RCS measurements of missiles 1, 2, 3, 4, and 5 respectively. Each figure includes a plot of the vertically and horizontally polarized incident field.

The measured values are converted to  $dB_{sm}$  for the purpose of display using 12, with a transmitted signal of  $E_t = 1[V/m^2]$ , and

$$RCS[dB] = 10 * \log \left( \frac{RCS[m^2]}{1[m^2]} \right). \quad (21)$$

The green wedge in each RCS cut represents the Angle-of-Interest (AOI), the region over which data is collected and used to train/evaluate the model. The total frequency content of each target over all angles are shown in figures 23-27. Again, figures are shown in  $RCS[dB_{sm}]$ , and represent the calibrated RCS measurements of missiles 1-5 respectively. Each figure include a plot of the vertically and horizontally polarized incident field.

The measurement result show a reduction in performance for all vertically polarized measurements. This is a defect in the instrumentation radar: the amplifier bank has been experiencing deteriorated performance due to a defect in the hardware. This was known prior to this research. However, this data has been collected anyway in an attempt to utilize the results to a limited extent, as well as potentially quantify the breakdown in performance.

### 4.3 Simulation Results

Figures 28-32 represent the simulated RCS of missiles 1-5 respectively. Each figure includes a plot of the vertically and horizontally polarized incident field.

As with the measurement data, each plot is converted to  $dB_{sm}$  using equations 12 and 21.

### 4.4 Data Comparison

The angular correlation between simulated and measured targets, augmented using the normalization routine, are presented in figures 33-37. Each figure shows the degree of correlation between one simulated target, and its correaltion with each

measured target. Figures list a separate correlation plot for horizontal and vertical polarizations.

On examination, Missile 1 (33) shows the strongest autocorrelation between simulation and measurement of all targets. The autocorrelation between the simulated targets shows progressively deteriorated performance moving from missile 1 to missile 5. In fact, the measurement data for missile 1 dominates the correlation results for missiles 2 and 3. The simulated results for missiles 2 and 3 (figures 34 and 35 respectively) show stronger correlation with missile 1, than with their own simulation. Missile 4 (figure 36) deviates from this trend, but only in the vertically polarized case. The horizontally polarized autocorrelation shows the worst performance of all models. Missile 5 shows poor autocorrelation in both polarizations. The strongest correlation for missile 5 is with missile 4's measurement data in vertical polarization.

As a measure of correlation performance versus signal to noise ratio, the correlation per angle was recalculated with additive noise applied to the simulation data. The average correlation product per target ( $\langle \rho \rangle$ ) over all angles is shown in figure 11.

As expected, the average correlation between the simulated and measured data increases with SNR. At a roughly  $28dB$ , correlation performance is flat. All targets show a near complete breakdown in correlation around  $6dB$ . Surprisingly, the vertically polarized measurements have a higher average correlation than expected. As noted previously, correlation performance degrades for successive targets. Missile 1's horizontally polarized autocorrelation shows the strongest performance with an average  $\rho$  of 0.892. This is followed by Missile 2's with an average  $\rho$  of 0.6. The remaining measurements show a range of  $\langle \rho \rangle$  between 0.6 and 0.08.

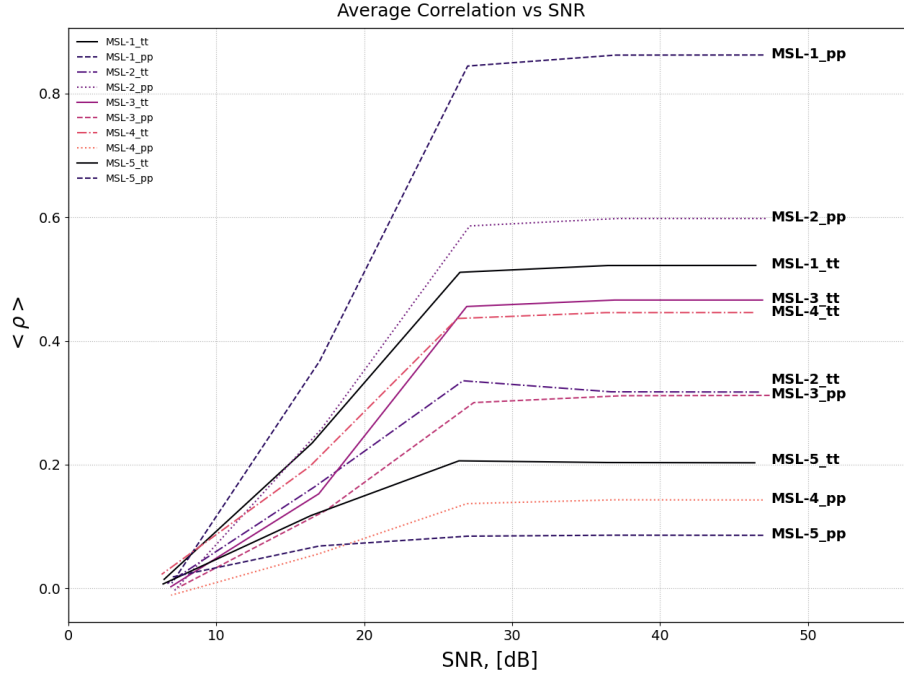


Figure 11: Top-down and side view of the AFIT compact radar range.

## 4.5 Model Evaluation

Multiple configurations were evaluated to find an optimal classifier network.

### 4.5.1 VGG-19

The VGG-19 classifier netowrk was developed by first identifying high-performing models. Model performance was determined by the calssification accuracy of the network for a given set of hyperparamters. Models with the highest overall accuracy were selected to be placed into a siamese network. The primary distinction of each model is the noise level that was applied to the training data. Conceptually, an array of models that have been trained on various noise levels would be able to accurately classify a signal in the presence of random noise, similar to a contested EMOE. The noise levels applied to the VGG-19 models were  $-5, 0, 5, 10$  [dBm].

For each given noise level, models were trained and evaluated using multiple hy-

perparamter configurations. The list of hyperparamters, and the values they were evaluated at are show in table 3. The VGG-19 was only able to converge when using the SGD optimizer, which was then used for the remainder of testing. The values of momentum are applicable to the SGD optimizer only.

Models were evaluated for their given training noise and hyperparamter config-ureations in “runs.” Each run is repeated five times to reduce statistical noise. The test results are shown in figure ??.

Table 3: List of test factors used to evaluate model performance.

Paramters	Value
Sample size	1000
	3000
	5000
Learning Rate	0.1
	0.01
	0.001
Batch Size	100
	200
	300
Optimizers	‘Adam’
	‘RMS Prop’
	‘SGD’
Momentum	0.5
	0.7
	0.9
Additive Noise Power	-20 [dBm]
	-10 [dBm]
	0 [dBm]
	10 [dBm]
	20 [dBm]

A preliminary evaluation of the listed hyperparameters was conducted to reduce the number of runs that would be required. Learning rates greater than 0.001 showed poor convergence, and resulted in failed classifications. The models using optimizers other than SGD were also unable to converge. The strongest performing models

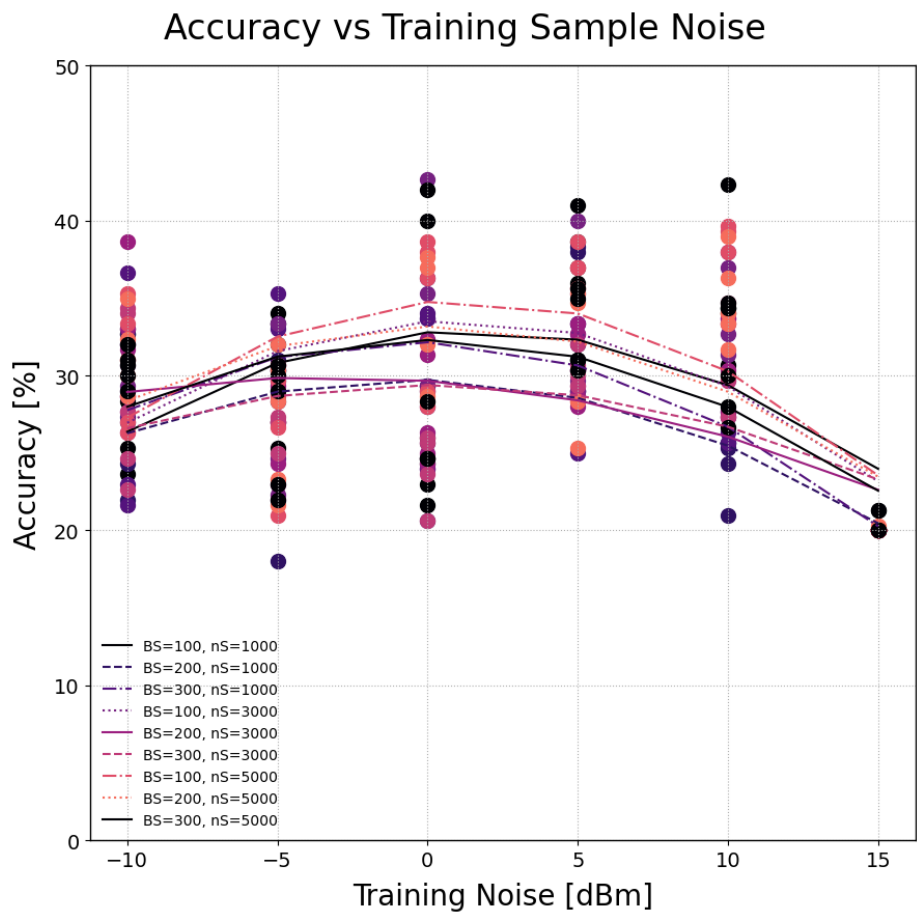


Figure 12: VGG-19 model performance using multiple hyperparameter configurations

utilized a batch size of 100, and sample size of 5000.

The top performing models were placed in siamese network, and re-evaluated using test data that has progressively large additive noise applied. The accuracy of the VGG-19 siamese network is shown in figure 13. Here, additive noise is applied to the test data, and passed to the network for evaluation. For each noise level, the network is tested 50 times and the average accuracy is reported. The network is baselined using simulation data first, and then reevaluated with measurement data. The averaged accuracy and classifier predictions are shown for each angle per SNR in figures 48-62.

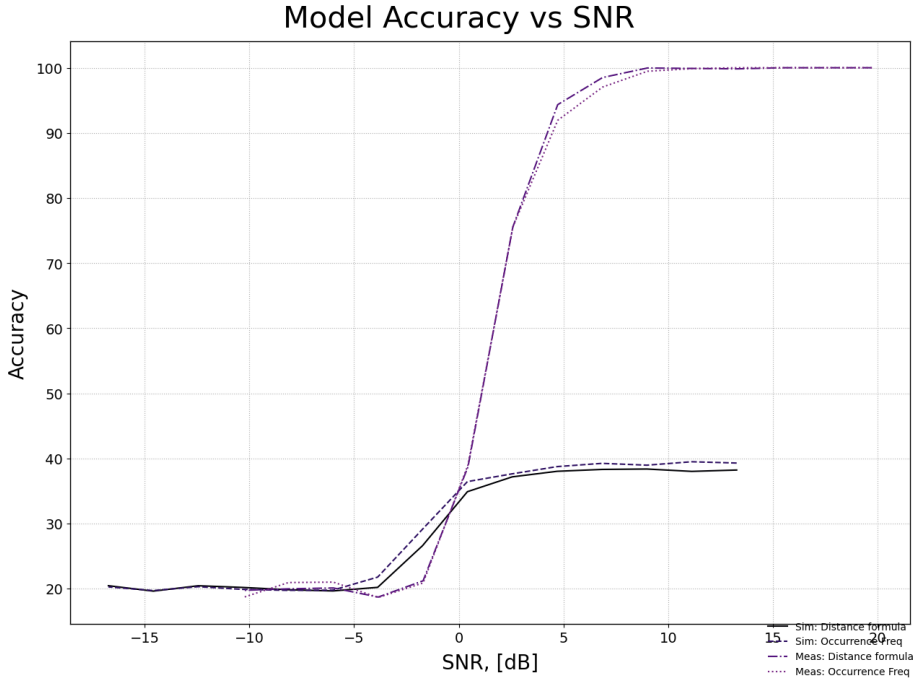


Figure 13: VGG-19 siamese netowrk performance versus SNR

Overall, performance is low for the measurement data. This is likely due to a host of factors. As noted previosly, the autocorrelation of simulated and measured missiles breakdown for missiles 3, 4, and 5. These breakdowns are captured in the confusion matrices of each model, shown in figures 43-47. The confusion matrices show a flaw in each of the models: *they tend to fixate on specific targets in order to increase*

*evaluation performance.* The most glaring example is shown in figure 43. This model features the highest evalutaion performance of the group, but completely neglects missiles 3 and 5. The problem of “fixation” is made more glaring when examining the number of classifications made by each model during their initial selection. Table ?? shows the percentage of calssifications made by each model when evaluating noiseless measurement data.

$$\begin{aligned}
 & \text{Missile 1:} 48\% \\
 & \text{Missile 2:} 33\% \\
 & \text{Missile 1:} 9\% \\
 & \text{Missile 1:} 59\% \\
 & \text{Missile 1:} 2\%
 \end{aligned} \tag{22}$$

In aggregate, the models favor missile 4 60% of the time they make a classification. This result is striking considering missile 4’s exceptionally weak correlation performance. This is likely due to strong correlation responses in the *training data*, shown in figures 38-42. There is strong cross correlation between missile 1, 2, and 3 as well as missiles 4 and 5.

The tendency towards target fixation is further confirmed when examining figures 54-62. The network latches onto missile 4 and heavily misreports the target. This becomes more pronounced as SNR decreases.

### 4.5.2 VGG-16

The VGG-19 system's depth prevented the network from generalizing the parameters of the model. This lack of generalization is suspected of creating the "target fixation" problem documented in the section 4.5.1. The simplified VGG-16 model serves as a potential cure.

The VGG-16 model was evaluated using the test matrix shown in table 5. The parameters of each run were evaluated recursively in-order to reduce statistical variation in the results.

The average performance per model versus applied training noise is shown in figure 14. The VGG-19 siamese network utilized only the strongest performing models from each run. In the interest of increasing the networks ability to generalize, *all* models generated from the runs listed in table 5 have been saved, and used to construct the network.

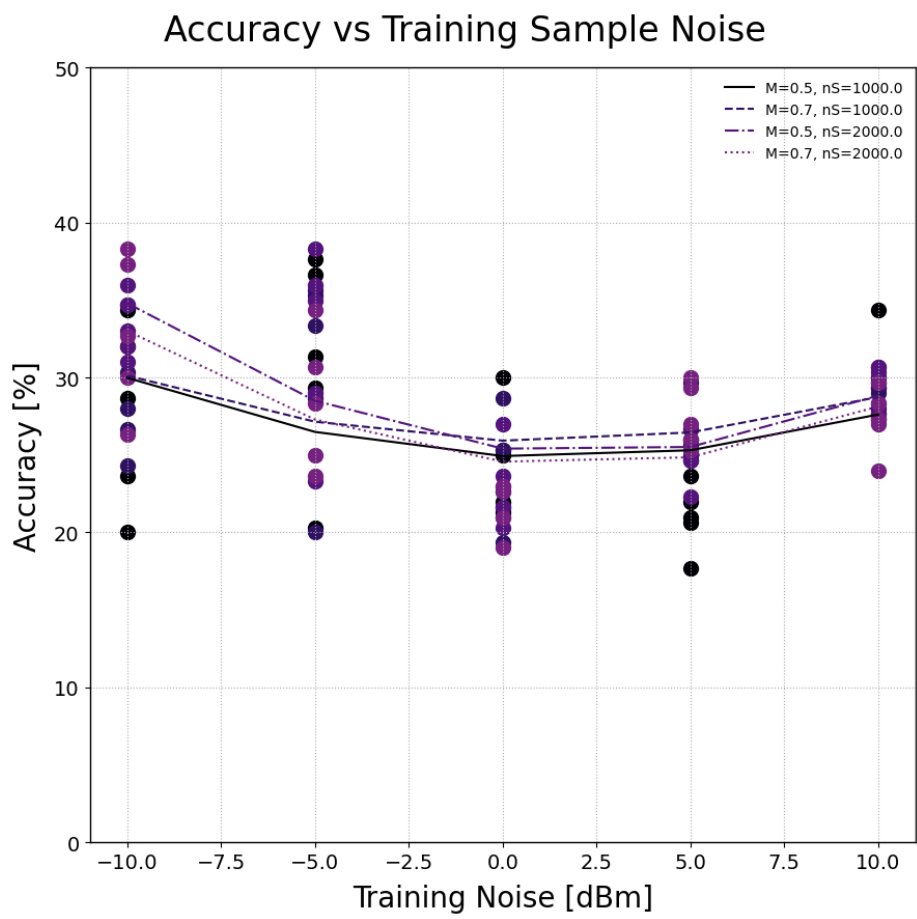


Figure 14: VGG-16 model performance.

## V. Conclusions

### 5.1 VGG-19

Choosing models based on the highest accuracy value did not prove to be a good approach. Models showed a tendency to fixate on specific targets, which gave a higher overall evaluation but a much lower ability to generalize.

Strong cross-correlation in the training data created confusion in the models ability to classify targets. Given the strong cross correlation between multiple targets, over multiple angles, the model was not able to create a generalized set of weights that allowed it to accurately make predictions.

Placing the models into a siamese network exacerbated the tendency towards target fixation.

### 5.2 VGG-16

### 5.3 Future Work

Text here

- Item 1 text here.
- Item 2 text here.

## Appendix A. Model Measurements

Name	Dimension	Unit [in]
fuselage	Length	18
	Diameter	3
	Fin	$2\frac{5}{16}$
Nose-1	Base	3
	Edge Length	$3\frac{11}{16}$
Nose-2	Base	3
	Edge Length	$5\frac{13}{16}$
Nose-3	Base	3
	Edge Length	$8\frac{11}{16}$
Nose-4	Base	3
	Diameter 1	2.91339
	Diameter 2	2.56
	Diameter 3	1.57
Nose-5	Base	3
	Diameter 1	2.87
	Diameter 2	2.52
	Diameter 3	1.89
	Diameter 3	0.83

Table 4: Model dimensions

## Appendix B. Models

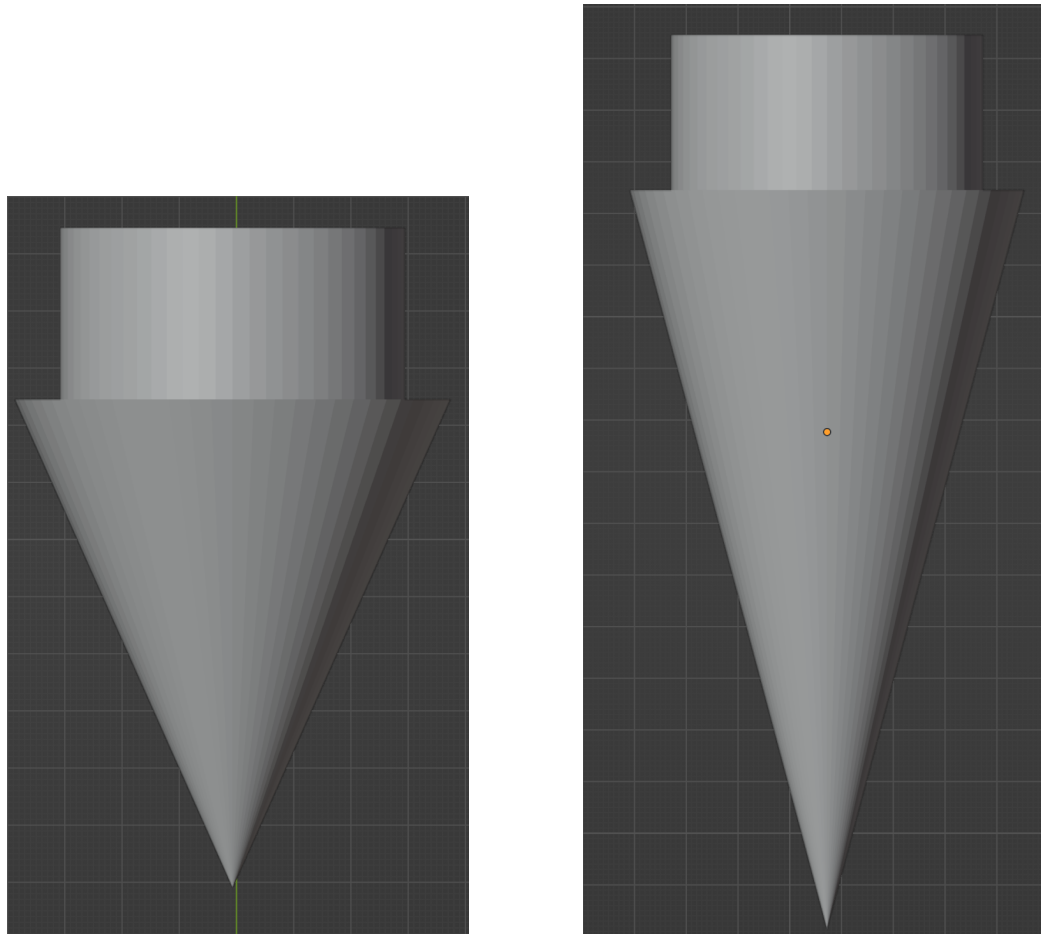


Figure 15: Simulation targets 1 and 2

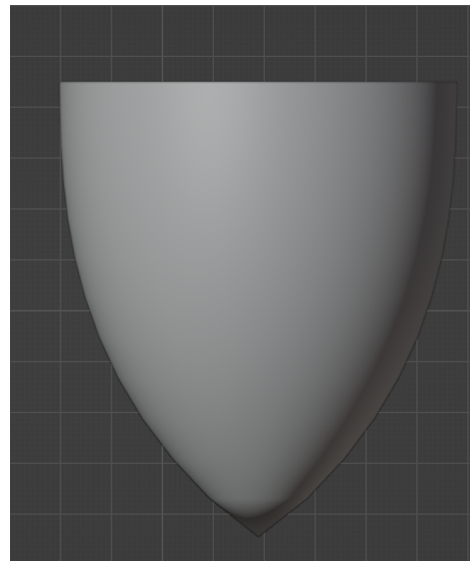
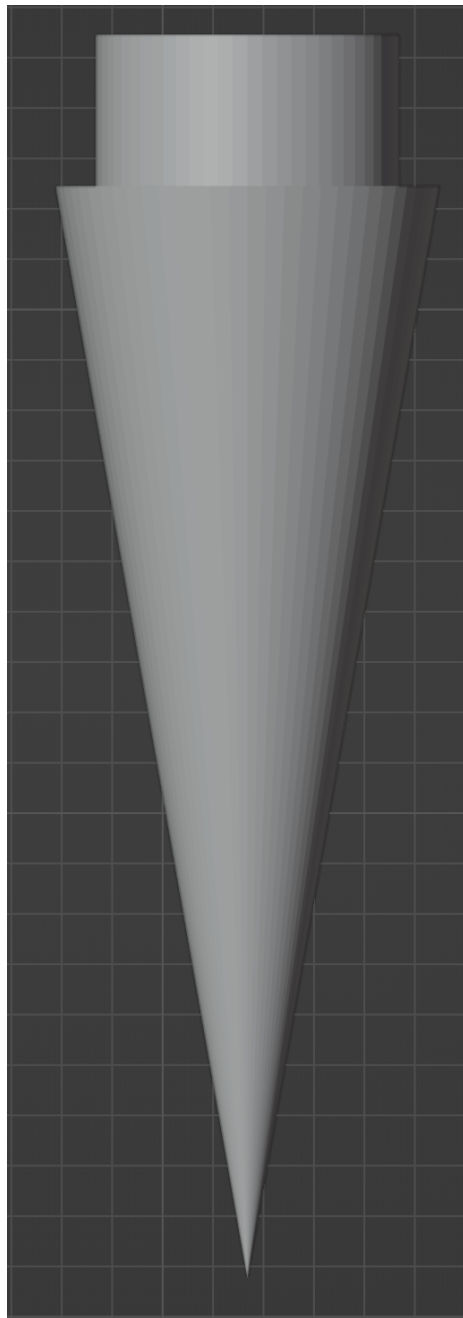


Figure 16: Simulation targets 3 and 4



Figure 17: Simulation targets 3 and 4

## Appendix C. Measurement Results

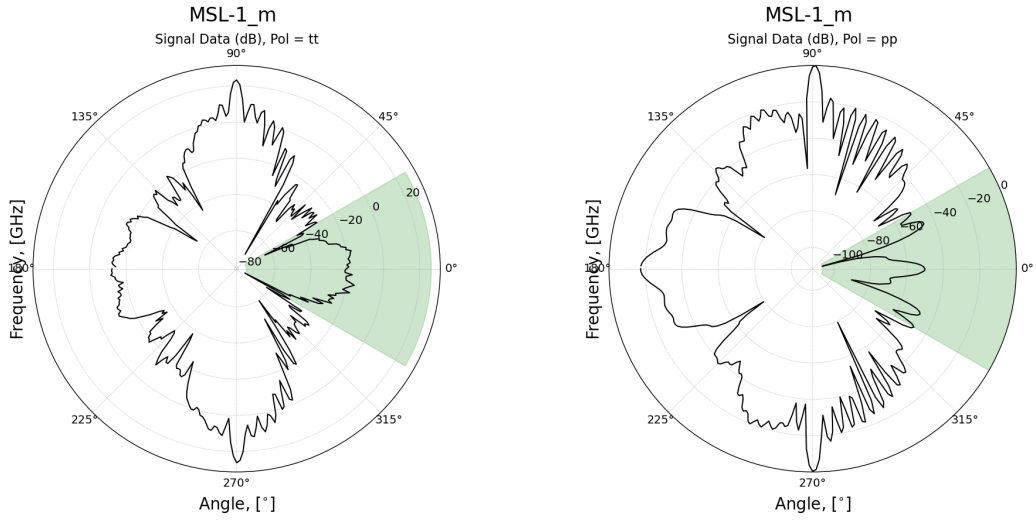


Figure 18: Missile 1 (Test): RCS cut at 5 GHz. Vertical (tt) and Horizontal (pp) polarizations

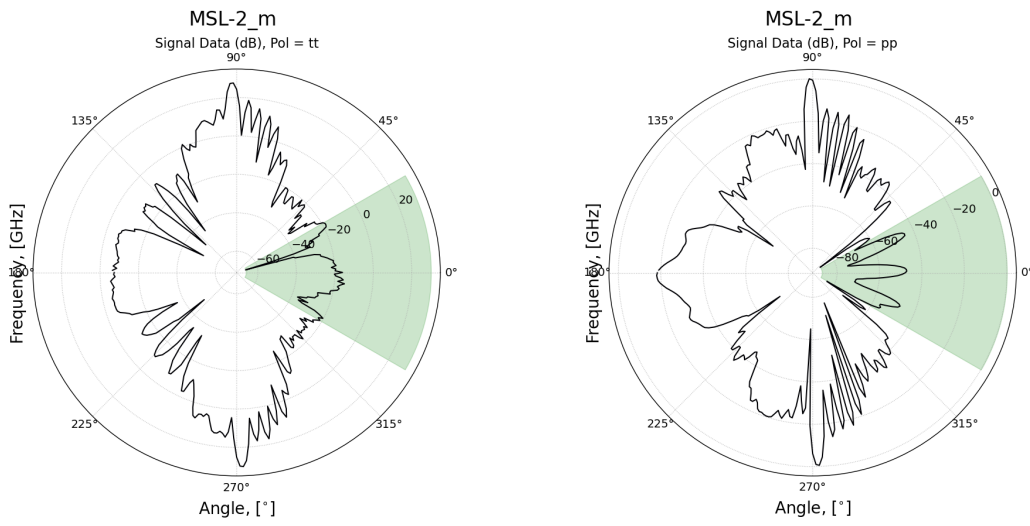


Figure 19: Missile 2 (Test): RCS cut at 5 GHz. Vertical (tt) and Horizontal (pp) polarizations

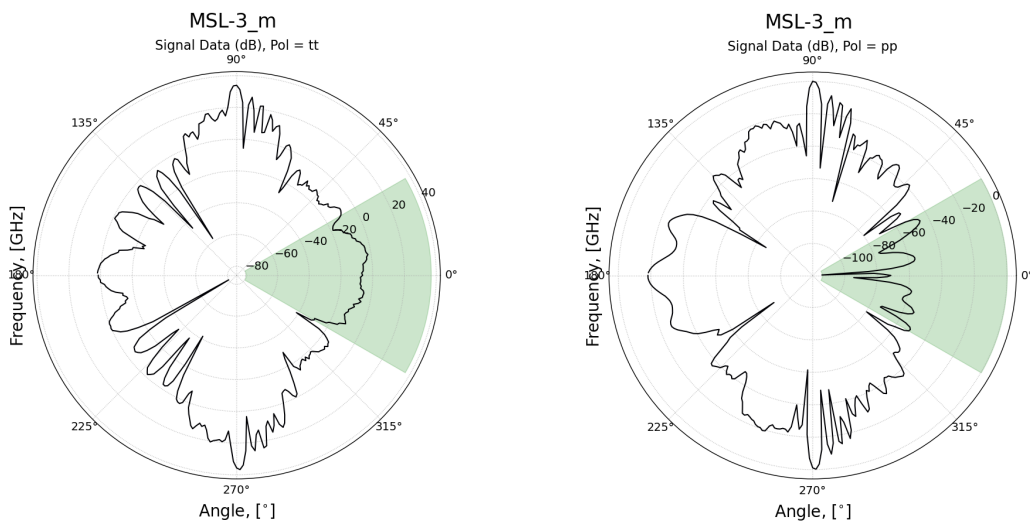


Figure 20: Missile 3 (Test): RCS cut at 5 GHz. Vertical (tt) and Horizontal (pp) polarizations

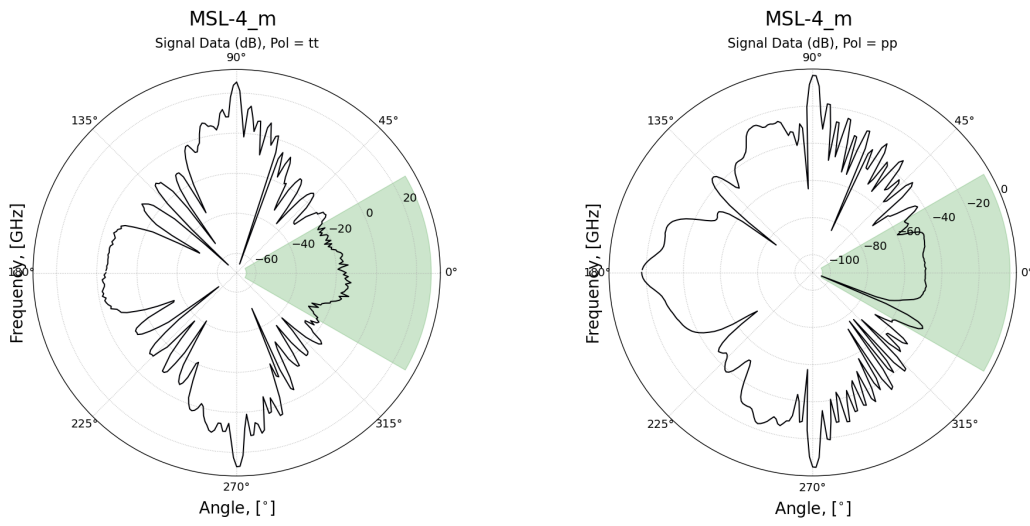


Figure 21: Missile 4 (Test): RCS cut at 5 GHz. Vertical (tt) and Horizontal (pp) polarizations

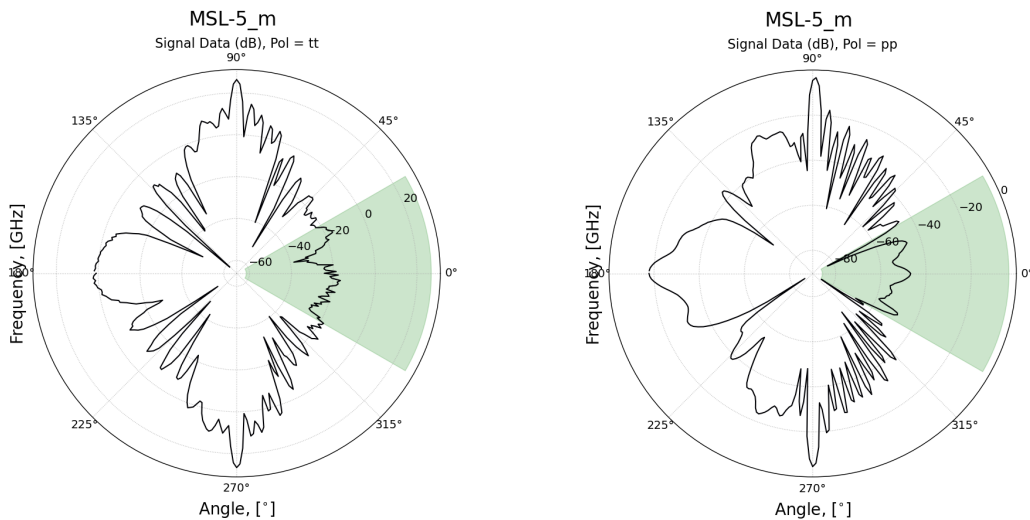


Figure 22: Missile 5 (Test): RCS cut at 5 GHz. Vertical (tt) and Horizontal (pp) polarizations

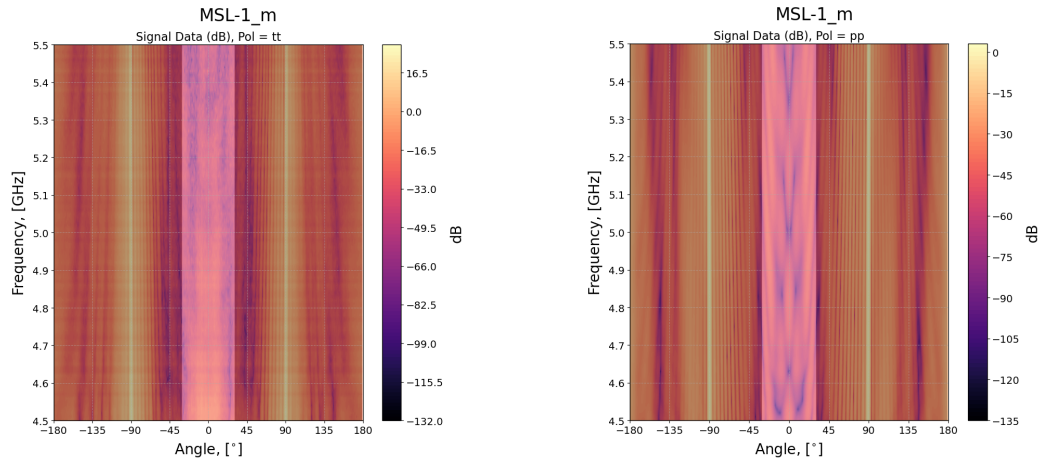


Figure 23: Missile 1 (Test): Total RCS. Vertical (tt) and Horizontal (pp) polarizations

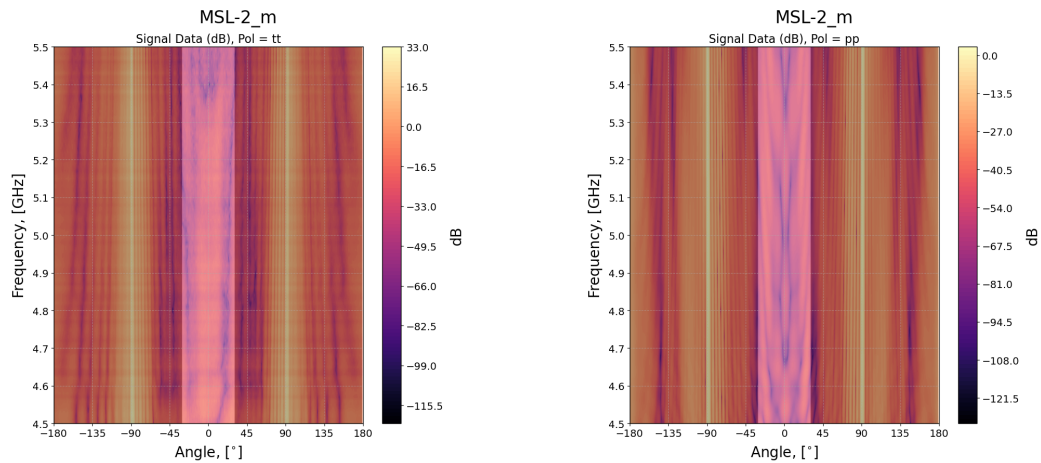


Figure 24: Missile 2 (Test): Total RCS. Vertical (tt) and Horizontal (pp) polarizations

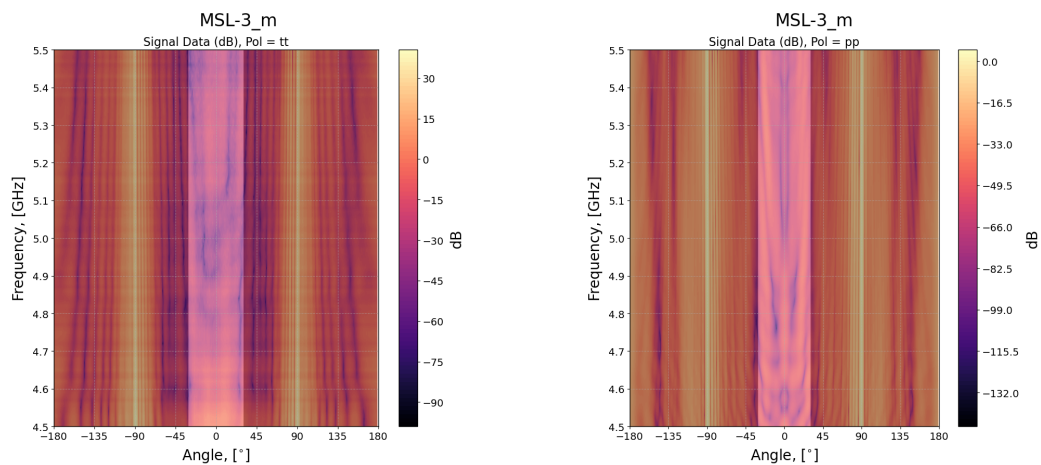


Figure 25: Missile 3 (Test): Total RCS. Vertical (tt) and Horizontal (pp) polarizations

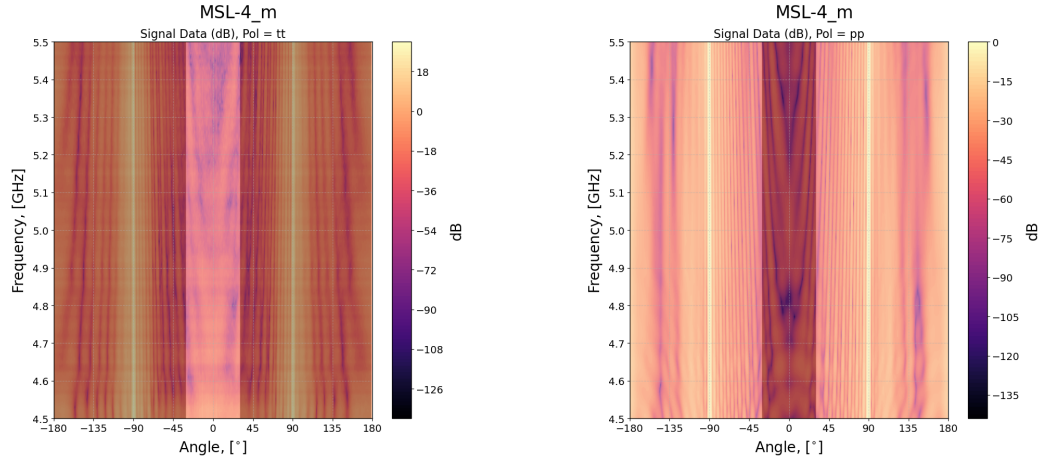


Figure 26: Missile 4 (Test): Total RCS. Vertical (tt) and Horizontal (pp) polarizations

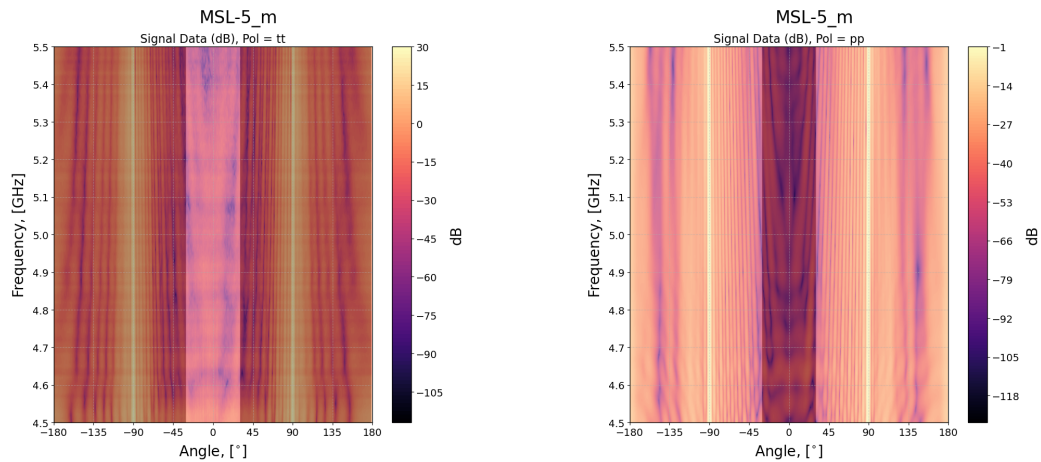


Figure 27: Missile 5 (Test): Total RCS. Vertical (tt) and Horizontal (pp) polarizations

## Appendix D. Simulation Results

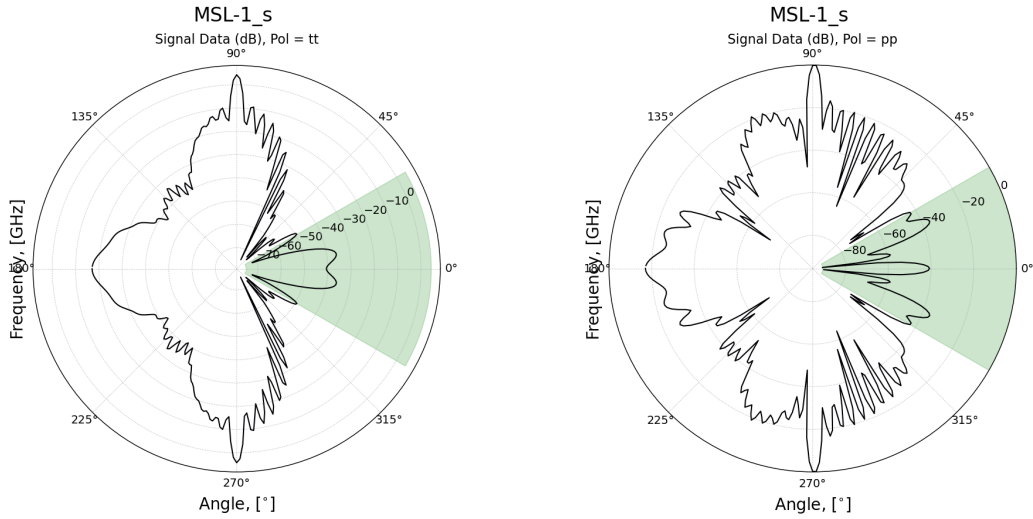


Figure 28: Missile 1 (**Sim**): RCS cut at 5 GHz. Vertical (tt) and Horizontal (pp) polarizations

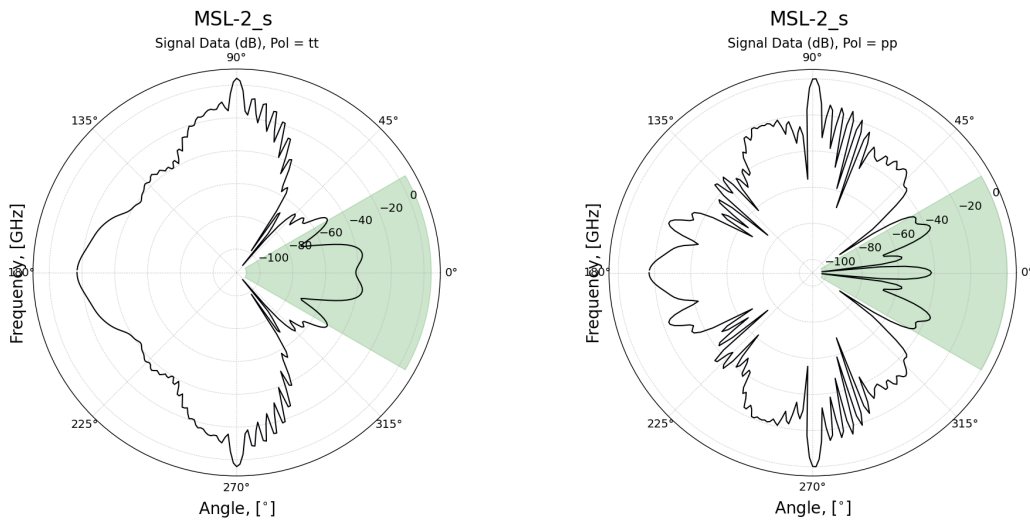


Figure 29: Missile 2 (Sim): RCS cut at 5 GHz. Vertical (tt) and Horizontal (pp) polarizations

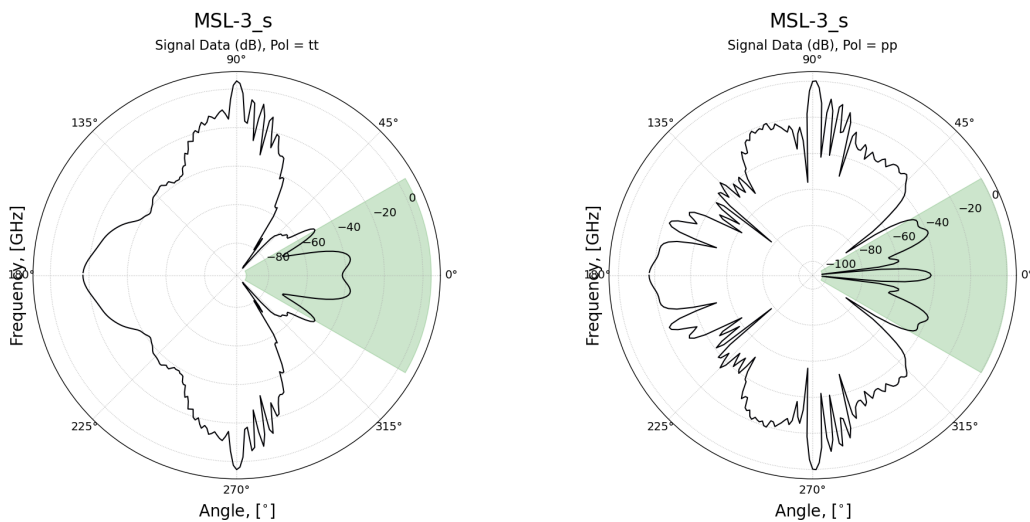


Figure 30: Missile 3 (Sim): RCS cut at 5 GHz. Vertical (tt) and Horizontal (pp) polarizations

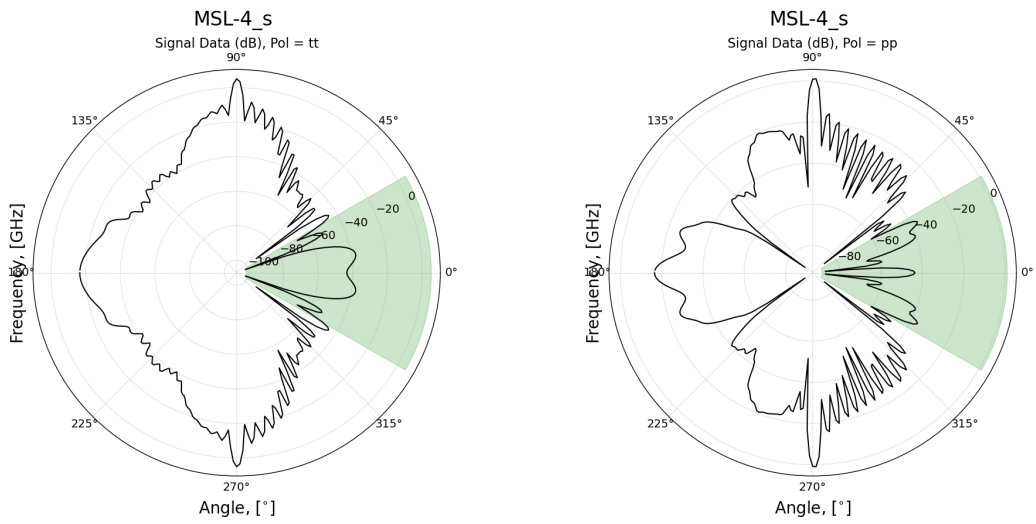


Figure 31: Missile 4 (Sim): RCS cut at 5 GHz. Vertical (tt) and Horizontal (pp) polarizations

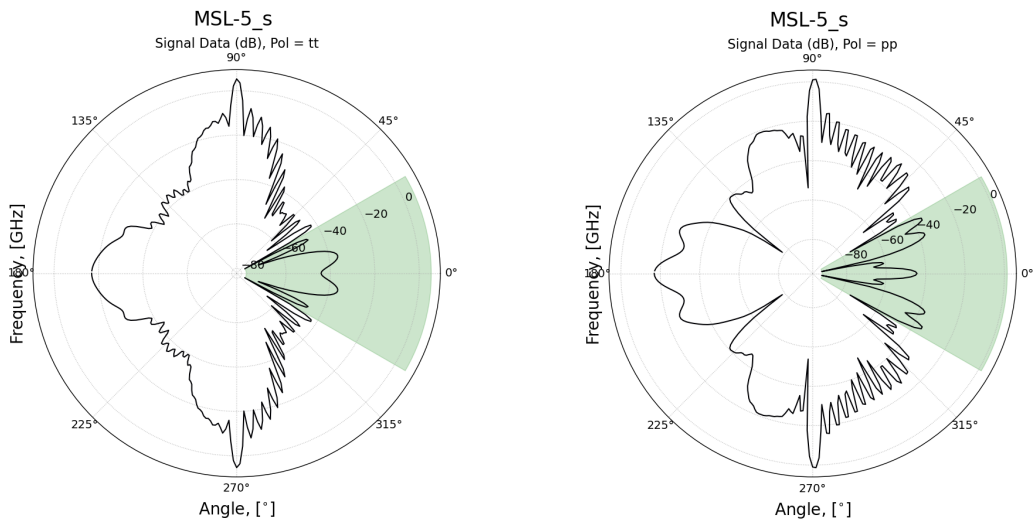


Figure 32: Missile 5 (Sim): RCS cut at 5 GHz. Vertical (tt) and Horizontal (pp) polarizations

## Appendix E. Correlation Results

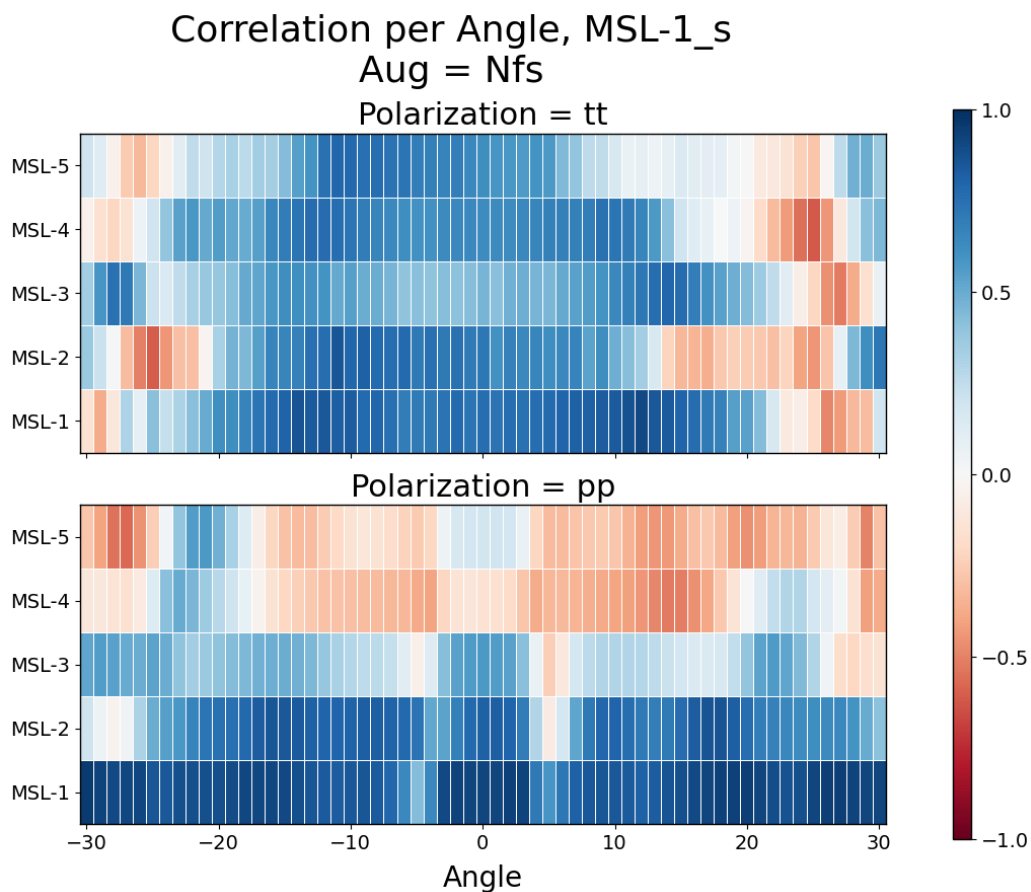


Figure 33: Correlation between the simulation of missile 1, and the measured RCS values for each target.

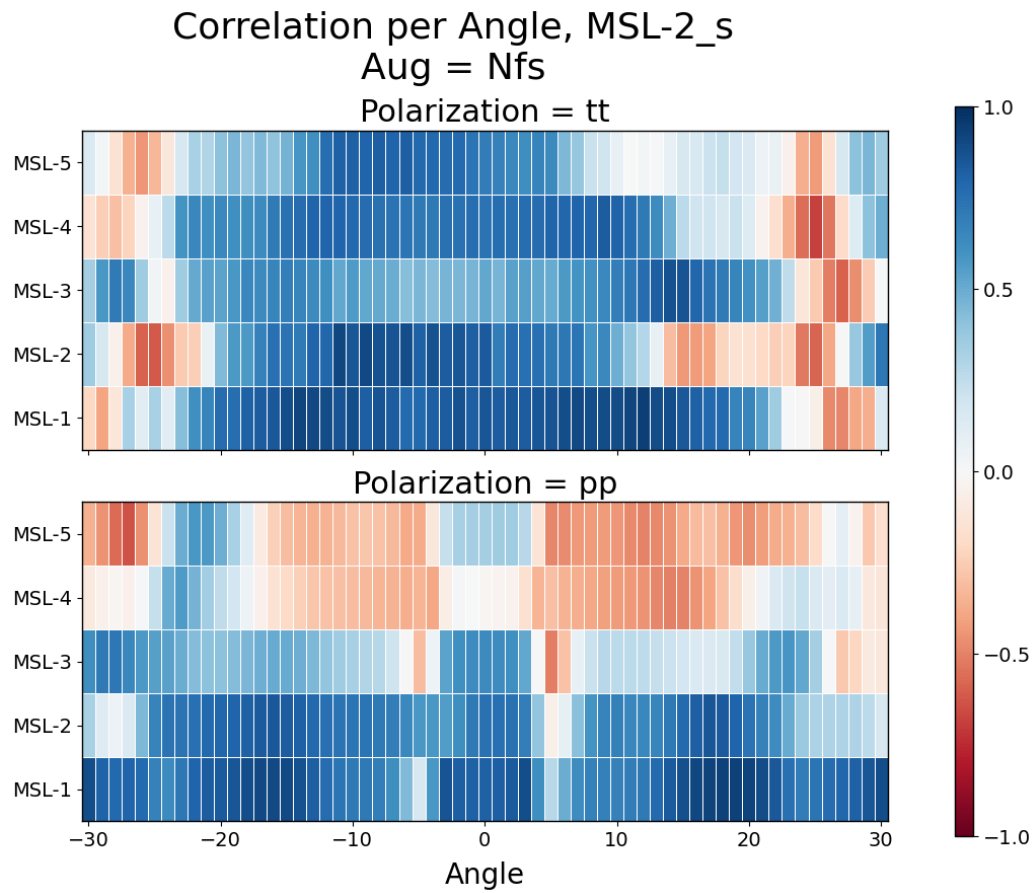


Figure 34: Correlation between the simulation of missile 2, and the measured RCS values for each target.

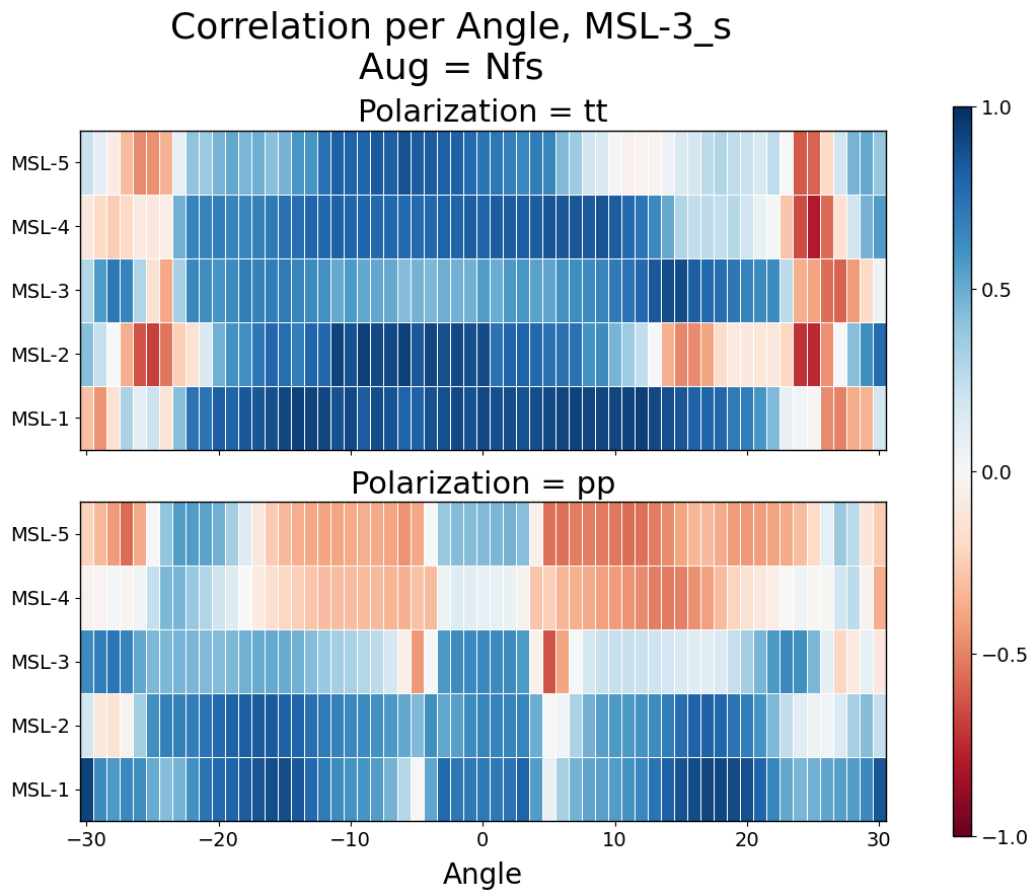


Figure 35: Correlation between the simulation of missile 3, and the measured RCS values for each target.

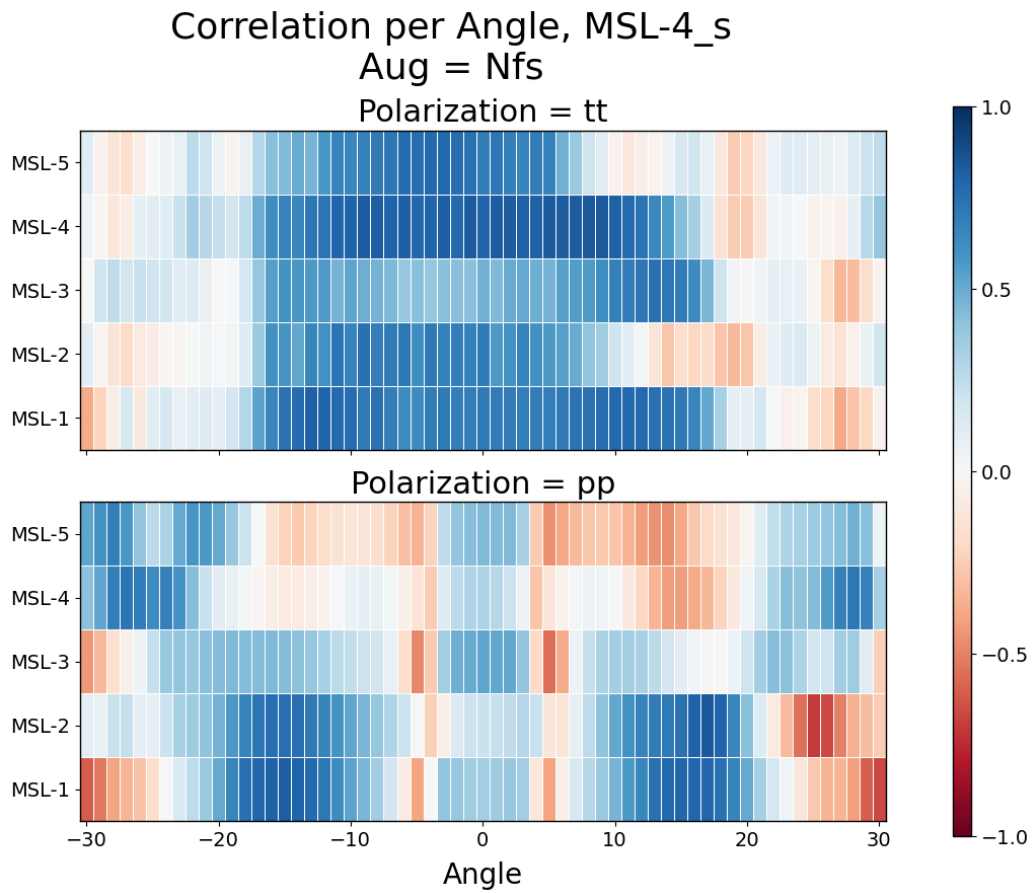


Figure 36: Correlation between the simulation of missile 4, and the measured RCS values for each target.

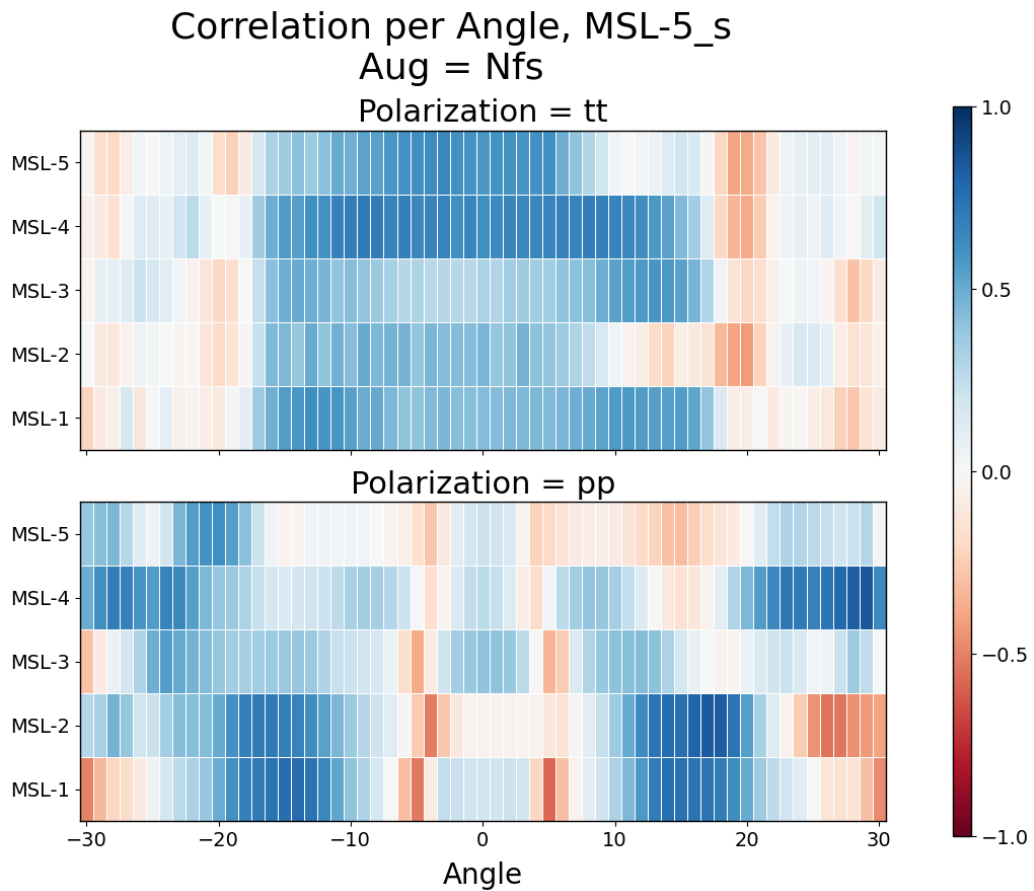


Figure 37: Correlation between the simulation of missile 5, and the measured RCS values for each target.

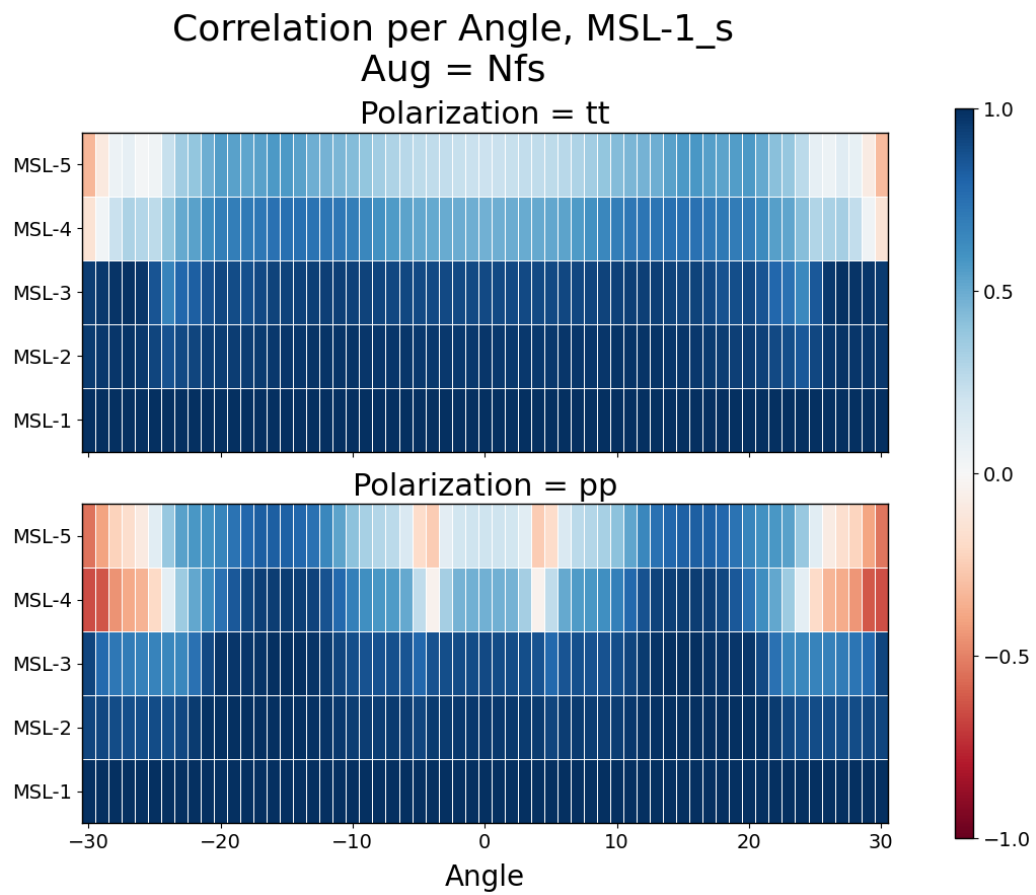


Figure 38: Correlation between the simulation of missile 1, and the simulated RCS values for each target.

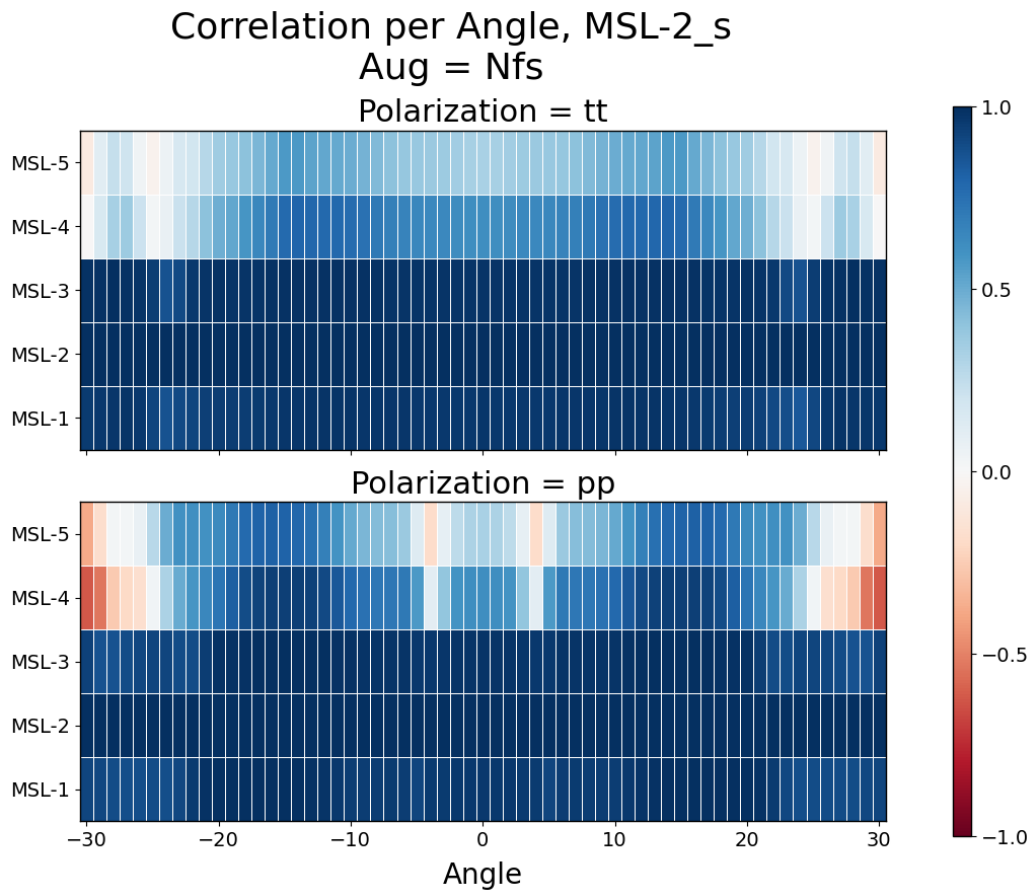


Figure 39: Correlation between the simulation of missile 2, and the simulated RCS values for each target.

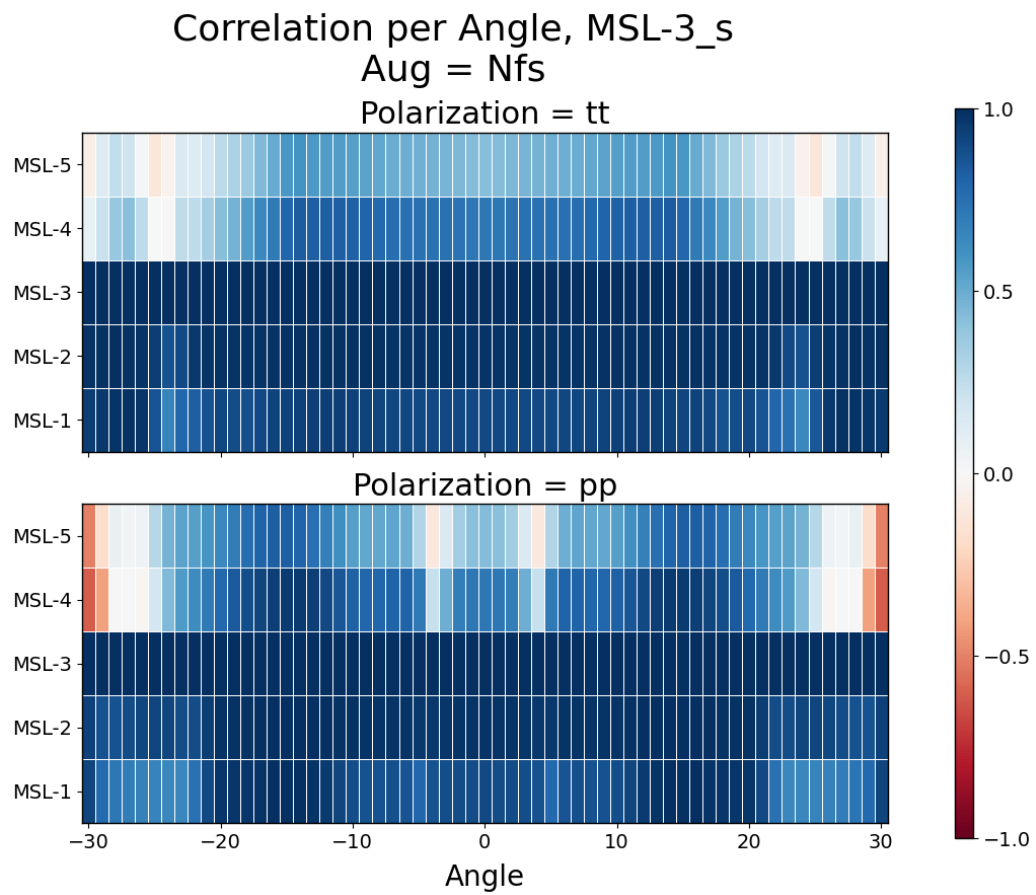


Figure 40: Correlation between the simulation of missile 3, and the simulated RCS values for each target.

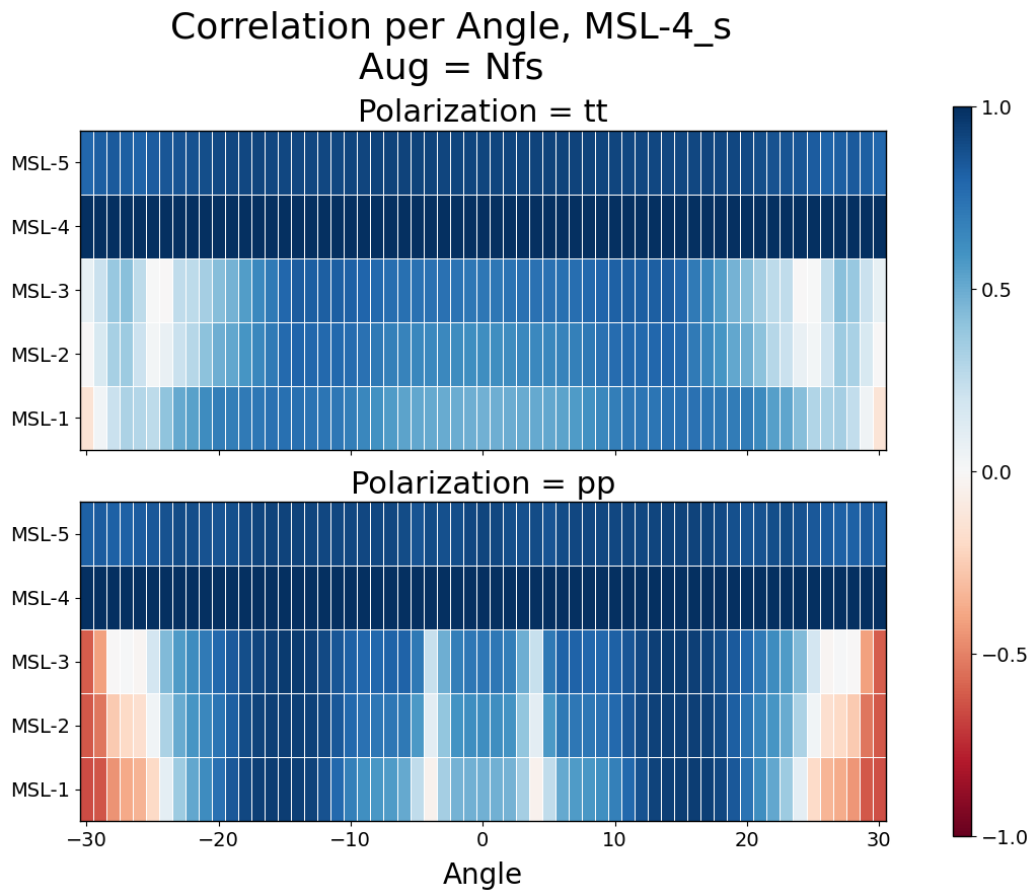


Figure 41: Correlation between the simulation of missile 4, and the simulated RCS values for each target.

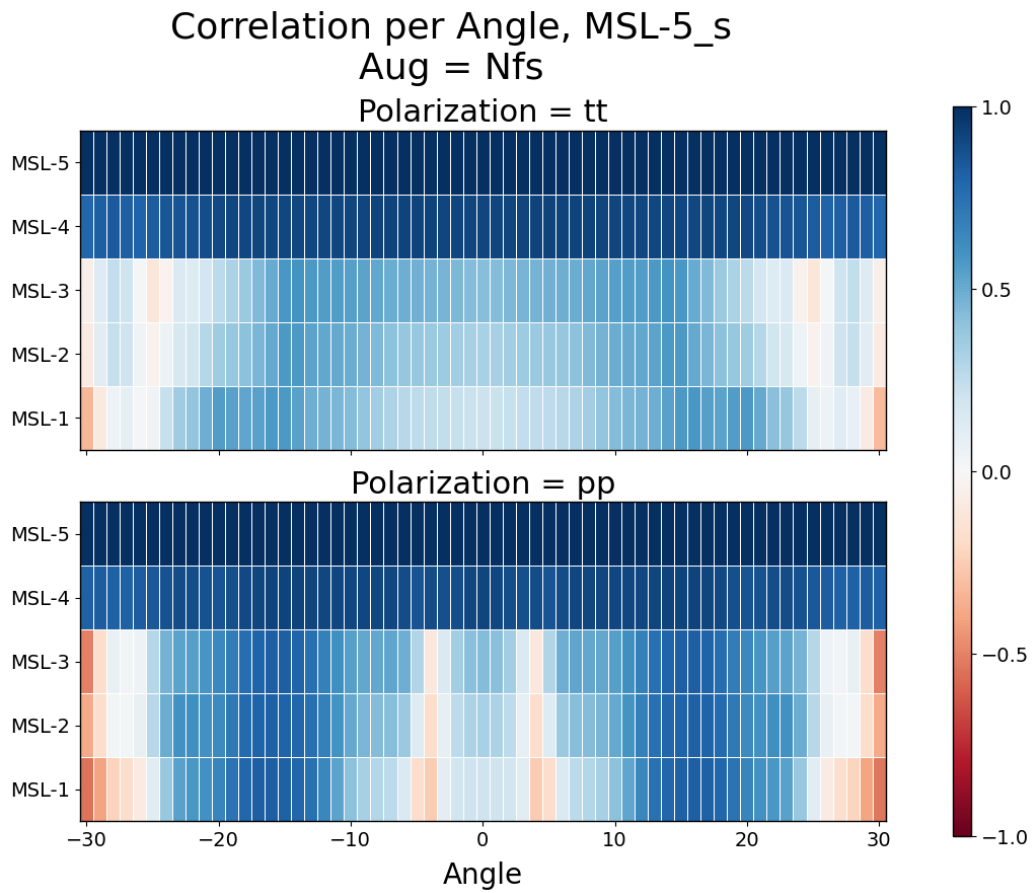


Figure 42: Correlation between the simulation of missile 5, and the simulated RCS values for each target.

## Appendix F. VGG-19 Results

### Confusion Matrix, Run 1

Batch Size= 100, Learning Rate= 0.001,  
nS= 5000, Label Category 0

Actual	Predicted					
	Nose-1	Nose-2	Nose-3	Nose-4	Nose-5	
Nose-1	40 13.33%	8 2.67%		12 4.00%		60 <b>66.67%</b> <b>33.33%</b>
Nose-2	23 7.67%	29 9.67%		8 2.67%		60 <b>48.33%</b> <b>51.67%</b>
Nose-3	4 1.33%	35 11.67%		21 7.00%		60 <b>0.00%</b> <b>100.00%</b>
Nose-4	3 1.00%	5 1.67%		50 16.67%	2 0.67%	60 <b>83.33%</b> <b>16.67%</b>
Nose-5	1 0.33%			59 19.67%		60 <b>0.00%</b> <b>100.00%</b>
	71 <b>56.34%</b> <b>43.66%</b>	77 <b>37.66%</b> <b>62.34%</b>	0 <b>0.00%</b> <b>0.00%</b>	150 <b>33.33%</b> <b>66.67%</b>	0 <b>0.00%</b> <b>100.00%</b>	300 <b>39.67%</b> <b>60.33%</b>

Figure 43: Confusion matrix for the -10 dBm model in the VGG-19 siamese network.

## Confusion Matrix, Run 2

Batch Size= 100, Learning Rate= 0.001,  
nS= 5000, Label Category 0

	Nose-1	Nose-2	Nose-3	Nose-4	Nose-5	
Nose-1	18 6.00%	11 3.67%	5 1.67%	22 7.33%	4 1.33%	60 <b>30.00%</b> <b>70.00%</b>
Nose-2	16 5.33%	32 10.67%	5 1.67%	5 1.67%	2 0.67%	60 <b>53.33%</b> <b>46.67%</b>
Nose-3	7 2.33%	31 10.33%	5 1.67%	17 5.67%		60 <b>8.33%</b> <b>91.67%</b>
Nose-4	9 3.00%			50 16.67%	1 0.33%	60 <b>83.33%</b> <b>16.67%</b>
Nose-5	19 6.33%			40 13.33%	1 0.33%	60 <b>1.67%</b> <b>98.33%</b>
	69 <b>26.09%</b> <b>73.91%</b>	74 <b>43.24%</b> <b>56.76%</b>	15 <b>33.33%</b> <b>66.67%</b>	134 <b>37.31%</b> <b>62.69%</b>	8 <b>12.50%</b> <b>87.50%</b>	300 <b>35.33%</b> <b>64.67%</b>
Predicted	Nose-1	Nose-2	Nose-3	Nose-4	Nose-5	

Figure 44: Confusion matrix for the -5 dBm model in the VGG-19 siamese network.

## Confusion Matrix, Run 3

Batch Size= 100, Learning Rate= 0.001,  
nS= 5000, Label Category 0

		Predicted				
		Nose-1	Nose-2	Nose-3	Nose-4	Nose-5
Actual	Nose-1	48 16.00%	7 2.33%		5 1.67%	60 <b>80.00%</b> <b>20.00%</b>
	Nose-2	41 13.67%	10 3.33%	2 0.67%	2 0.67%	5 1.67%
	Nose-3	20 6.67%	16 5.33%	11 3.67%	13 4.33%	60 <b>18.33%</b> <b>81.67%</b>
	Nose-4	4 1.33%	1 0.33%		38 12.67%	17 5.67%
	Nose-5	13 4.33%	1 0.33%	5 1.67%	36 12.00%	5 1.67%
		<b>126</b> <b>38.10%</b> <b>61.90%</b>	<b>35</b> <b>28.57%</b> <b>71.43%</b>	<b>18</b> <b>61.11%</b> <b>38.89%</b>	<b>89</b> <b>42.70%</b> <b>57.30%</b>	<b>300</b> <b>15.62%</b> <b>84.38%</b>

Figure 45: Confusion matrix for the 0 dBm model in the VGG-19 siamese network.

## Confusion Matrix, Run 4

Batch Size= 100, Learning Rate= 0.001,  
nS= 5000, Label Category 0

	Predicted					
Actual	Nose-1	Nose-2	Nose-3	Nose-4	Nose-5	
Nose-1	38 12.67%	20 6.67%		2 0.67%		60 <b>63.33%</b> <b>36.67%</b>
Nose-2	26 8.67%	27 9.00%	6 2.00%	1 0.33%		60 <b>45.00%</b> <b>55.00%</b>
Nose-3	9 3.00%	31 10.33%	11 3.67%	9 3.00%		60 <b>18.33%</b> <b>81.67%</b>
Nose-4	8 2.67%	13 4.33%		39 13.00%		60 <b>65.00%</b> <b>35.00%</b>
Nose-5	12 4.00%	16 5.33%	8 2.67%	24 8.00%		60 <b>0.00%</b> <b>100.00%</b>
	93 <b>40.86%</b> <b>59.14%</b>	107 <b>25.23%</b> <b>74.77%</b>	25 <b>44.00%</b> <b>56.00%</b>	75 <b>52.00%</b> <b>48.00%</b>	0 <b>0.00%</b> <b>0.00%</b>	300 <b>38.33%</b> <b>61.67%</b>

Figure 46: Confusion matrix for the 5 dBm model in the VGG-19 siamese network.

## Confusion Matrix, Run 5

Batch Size= 100, Learning Rate= 0.001,  
nS= 5000, Label Category 0

Actual	Predicted					Total
	Nose-1	Nose-2	Nose-3	Nose-4	Nose-5	
Nose-1	11 3.67%	13 4.33%	5 1.67%	26 8.67%	5 1.67%	60 <b>18.33%</b> <b>81.67%</b>
Nose-2	15 5.00%	28 9.33%	4 1.33%	11 3.67%	2 0.67%	60 <b>46.67%</b> <b>53.33%</b>
Nose-3	7 2.33%	22 7.33%	2 0.67%	29 9.67%		60 <b>3.33%</b> <b>96.67%</b>
Nose-4	7 2.33%			51 17.00%	2 0.67%	60 <b>85.00%</b> <b>15.00%</b>
Nose-5	21 7.00%			36 12.00%	3 1.00%	60 <b>5.00%</b> <b>95.00%</b>
	<b>61</b> <b>18.03%</b> <b>81.97%</b>	<b>63</b> <b>44.44%</b> <b>55.56%</b>	<b>11</b> <b>18.18%</b> <b>81.82%</b>	<b>153</b> <b>33.33%</b> <b>66.67%</b>	<b>12</b> <b>25.00%</b> <b>75.00%</b>	<b>300</b> <b>31.67%</b> <b>68.33%</b>

Figure 47: Confusion matrix for the 10 dBm model in the VGG-19 siamese network.

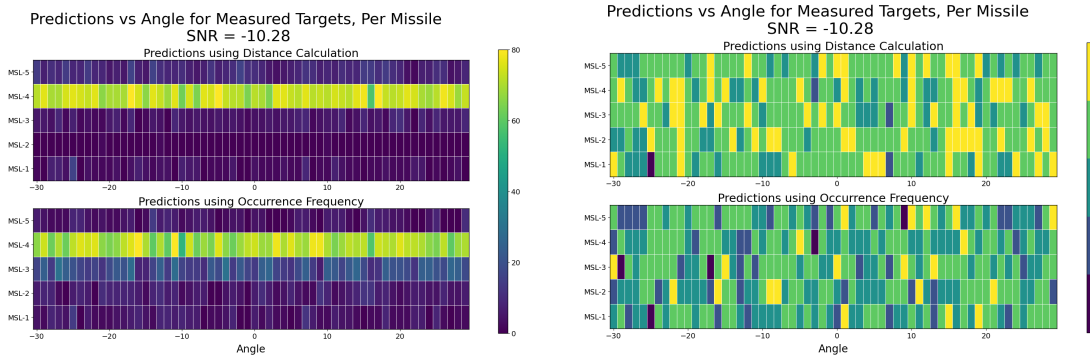


Figure 48: Angle accuracy and Classification for the VGG-19 siamese network, SNR=-10 dB

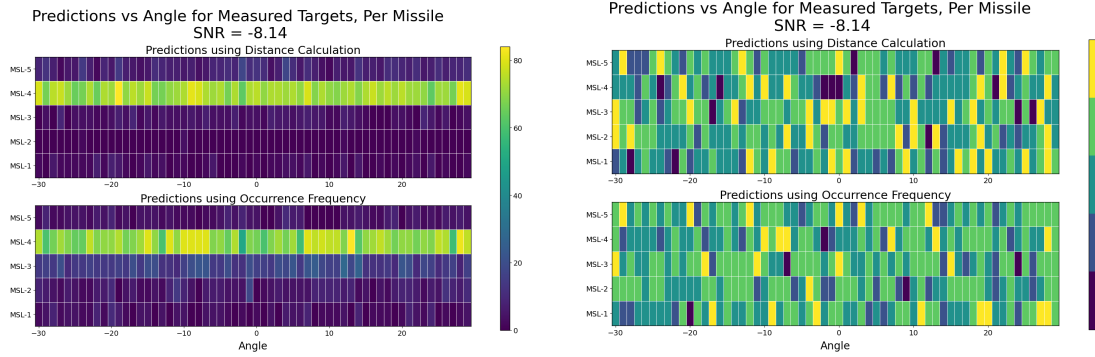


Figure 49: Angle accuracy and Classification for the VGG-19 siamese network, SNR= -8 dB

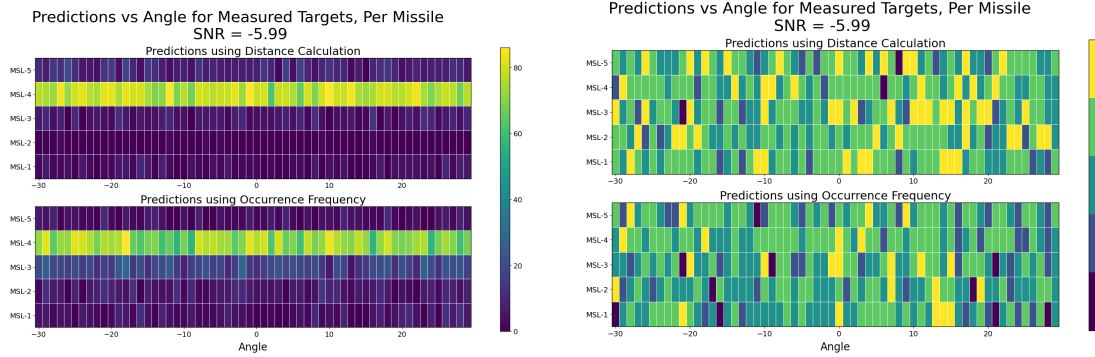


Figure 50: Angle accuracy and Classification for the VGG-19 siamese network, SNR= -6 dB

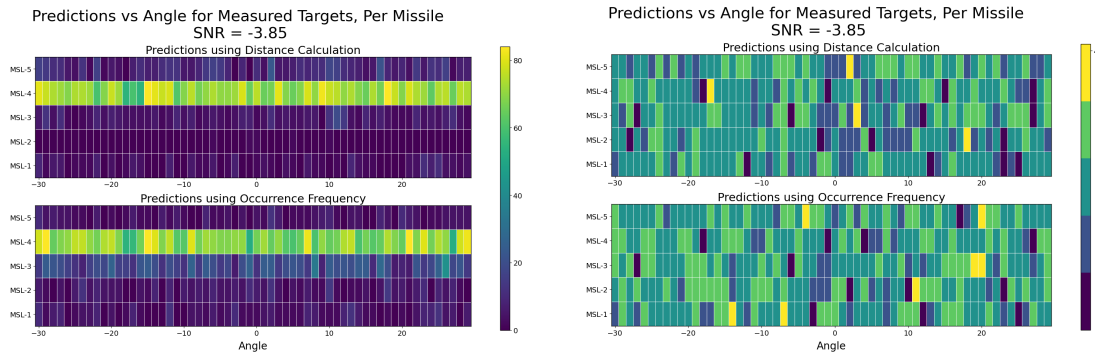


Figure 51: Angle accuracy and Classification for the VGG-19 siamese network, SNR= -4 dB

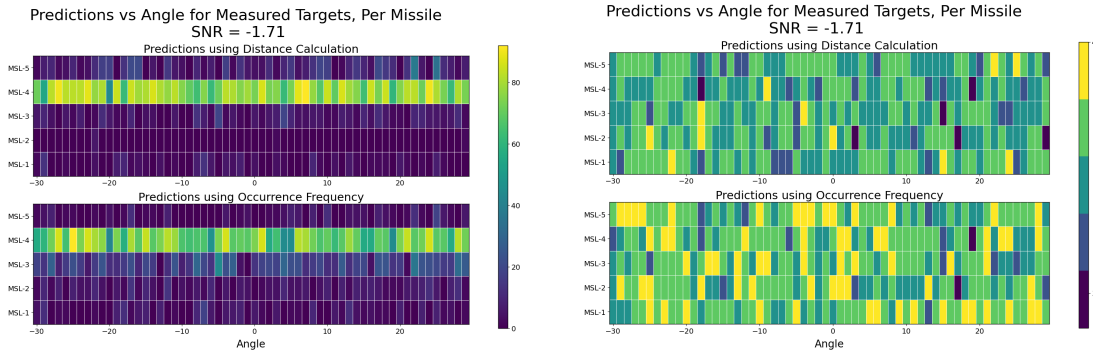


Figure 52: Angle accuracy and Classification for the VGG-19 siamese network, SNR=-2 dB

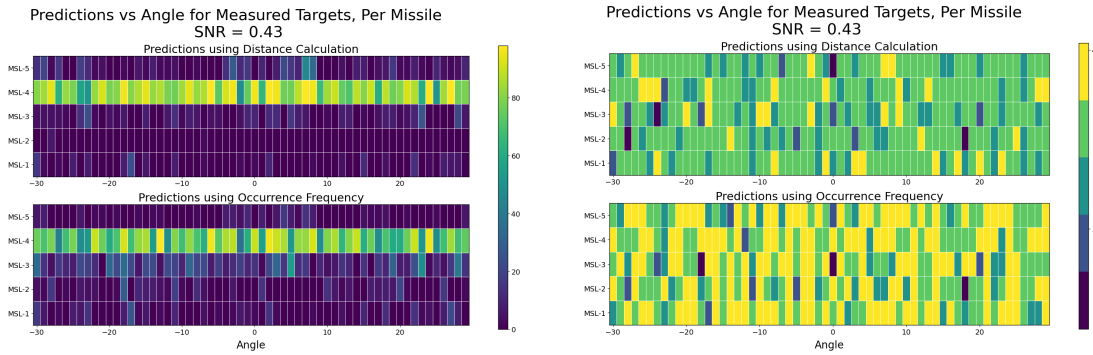


Figure 53: Angle accuracy and Classification for the VGG-19 siamese network, SNR=0 dB

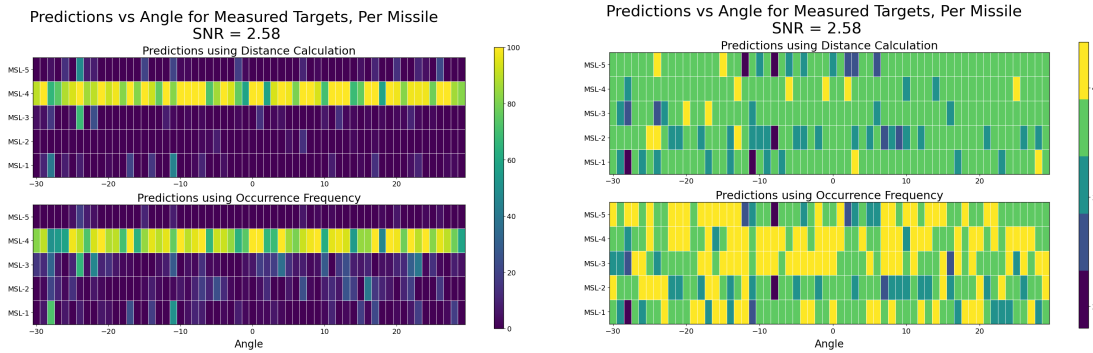


Figure 54: Angle accuracy and Classification for the VGG-19 siamese network, SNR=3 dB

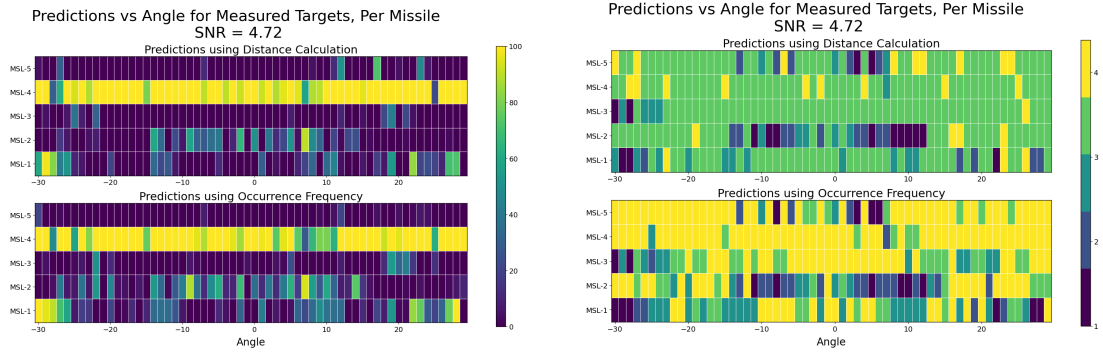


Figure 55: Angle accuracy and Classification for the VGG-19 siamese network, SNR=5 dB

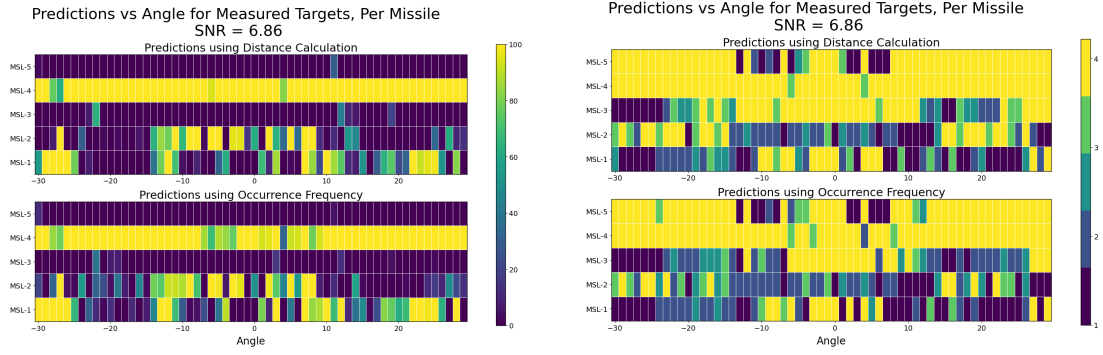


Figure 56: Angle accuracy and Classification for the VGG-19 siamese network, SNR=7 dB

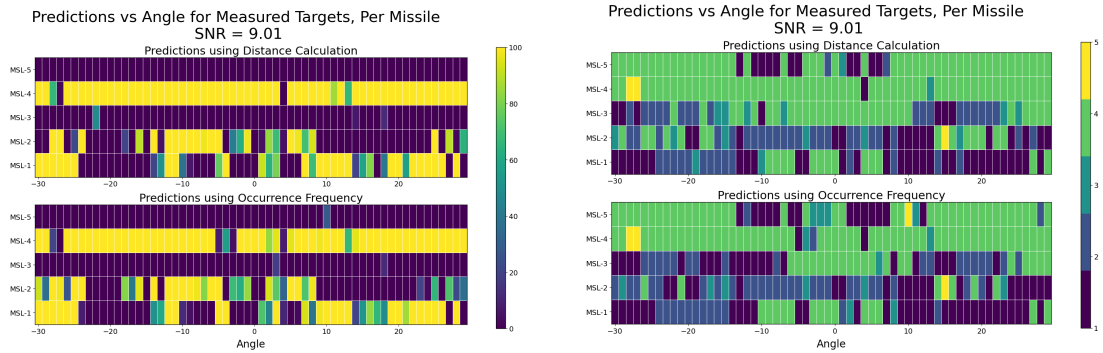


Figure 57: Angle accuracy and Classification for the VGG-19 siamese network, SNR=9 dB

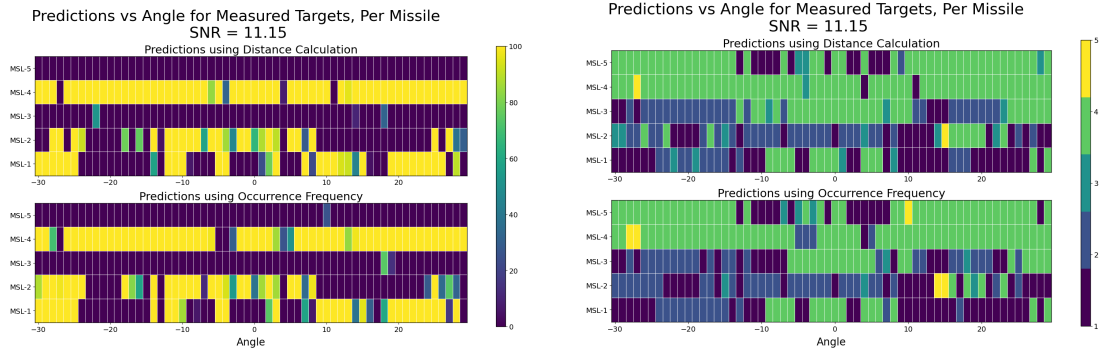


Figure 58: Angle accuracy and Classification for the VGG-19 siamese network, SNR=11 dB

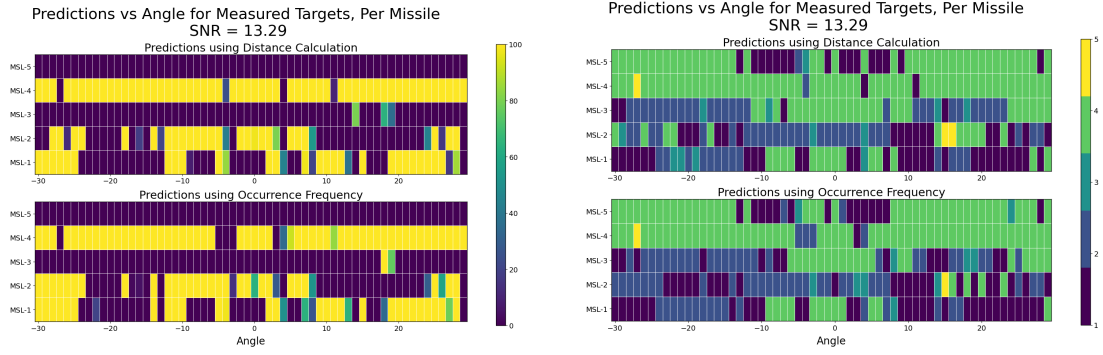


Figure 59: Angle accuracy and Classification for the VGG-19 siamese network, SNR=13 dB

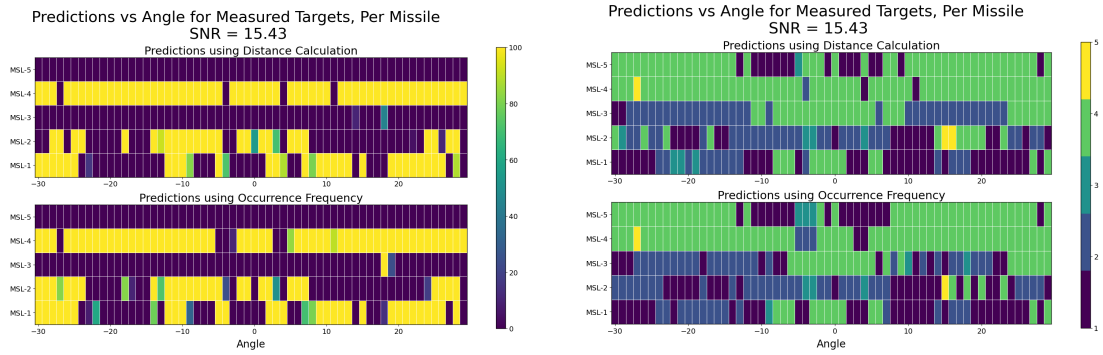


Figure 60: Angle accuracy and Classification for the VGG-19 siamese network, SNR=15 dB

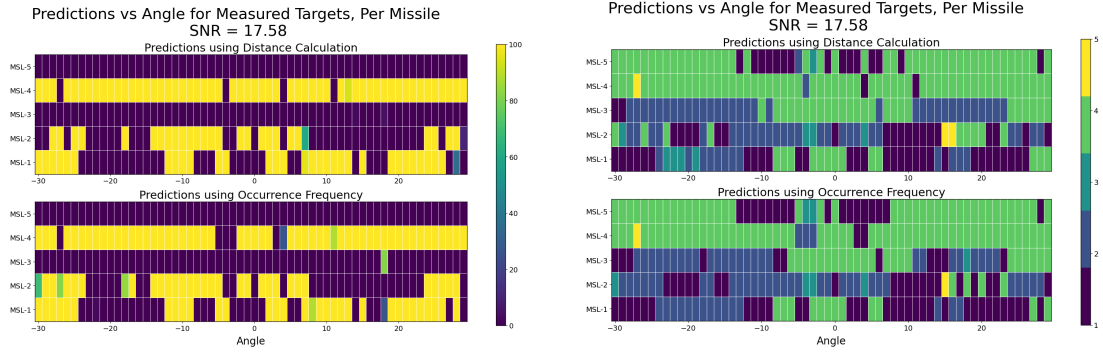


Figure 61: Angle accuracy and Classification for the VGG-19 siamese network, SNR=18 dB

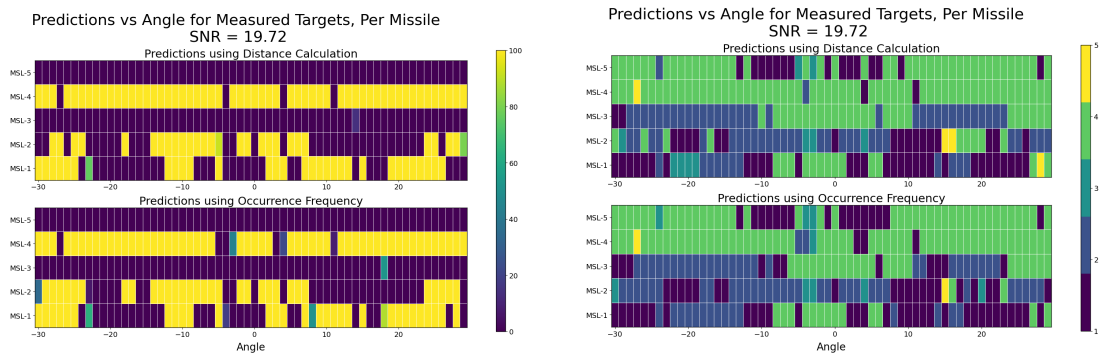


Figure 62: Angle accuracy and Classification for the VGG-19 siamese network, SNR=20 dB

## Appendix G. VGG-16 Results

Run number	Sample Size	Training Noise [dBm]	Momentum
1	2000	0.5	-5
2	2000	0.7	-10
3	1000	0.7	10
4	1000	0.5	-5
5	2000	0.5	-10
6	1000	0.7	-5
7	2000	0.7	0
8	2000	0.5	0
9	1000	0.5	0
10	2000	0.7	-5
11	2000	0.5	10
12	1000	0.7	-10
13	2000	0.5	5
14	1000	0.5	10
15	1000	0.5	-10
16	1000	0.5	5
17	2000	0.7	10
18	1000	0.7	0
19	1000	0.7	5
20	2000	0.7	5

Table 5: VGG-16 test card listing the evaluated configurations of the network.

## Bibliography

1. R. M. Hoffer. 2020 Department of Defense Electromagnetic Spectrum Superiority Strategy. US Department of Defense <https://www.defense.gov/News/Releases/Release/Article/2397850/electromagnetic-spectrum-superiority-strategy-released/>. (Accessed: 30 August 2022).
2. Naval Gazing. Aerial decoys. Naval Gazing <https://www.navalgazing.net/Aerial-Decoys>. (Accessed: 1 Dec 2022).
3. Jin Au Kong. *Electromagnetic Wave Theory*. EMW Publishing, 2000.
4. E. G. Bowen. *Radar Days*. Intitute of Phsyics Publishing, 1987.
5. M. A. Richards, J. A. Scheer, and W. A. Holm. *Noise*, pages 61–65. Scitech Publishing, Edison, NJ, 2010.
6. Eugene Knott. *Radar Cross Section*. Scitech Publishing, Raleigh, NC, 2004.
7. M. A. Richards, J. A. Scheer, and W. A. Holm. *Noise*, pages 64–66. Scitech Publishing, Edison, NJ, 2010.
8. J. B. Johnson. Thermal agitation of electricity in conductors. *Physical Review*, 32:97–109, 1928.
9. H. Nyquist. Thermal agitation of electric charge in conductors\*. *Physical Review*, 32:110–113, 1928.
10. Francois Chollet. *Deep Learning with Python*. Manning Publications, 2018.
11. Ping Lang, Xiongjun Fu, Jian Dong, Rui Qin, Xiapeng Meng, and Min Xie. A comprehensive survey of machine learning applied to radar signal processing. *IEEE Access*, 10(10), 2020.

12. Eric Wengrowski, Matthew Purri, Kristin Dana, and Andrew Huston. Deep convolutional neural networks as a method to classify rotating objects based on monostatic radar cross section, 2018.
13. Zewen Li, Wenjie Yang, Shouheng Peng, and Fan Liu. A survey of convolutional neural networks: Analysis, applications, and prospects. *arXiv*, 2020.
14. W. McCulloch and W. Pitts. A logical calculus of ideas immanent in nervous activity. *Bulletin of Mathematical Physics*, 1943.
15. Aurelien. *Hands on Machine Learning with Scikit-Learn, Keras and TensorFlow*. O'Reilly Media, 2019.
16. D. E. Rumelhart, G. E. Hinton, and R. J. Williams. Learning internal representation by error propagation, 1986.
17. *Proc. International Conference on Learning Representations 2015*. arXiv, 2015.
18. Keras Functional API Documentation. Keras functional api documentation. Keras <https://keras.io/api>. (Accessed: 1 Dec 2022).
19. Khalid El-Darymli, Eric W. Gill, Peter McGuire, Desmond Power, and Cecilia Moloney. Automatic target recognition in synthetic aperture radar imagery: A state-of-the-art review. *IEEE Access*, 4:6014–6058, 2016.
20. H. S. Truman. Executive order 10290. The American Presidency Project <https://www.presidency.ucsb.edu/node/278445>. (Accessed: 9 Sept 2022).
21. C. Campbell. China's military: The people's liberation army. Congressional Research Service <https://crsreports.congress.gov/product/pdf/R/R46808>. (Accessed: 9 Sept 2022).

22. M. A. Dennis. Rodney brooks. Britannica <https://www.britannica.com/biography/Rodney-Allen-Brooks>. (Accessed: 9 Sept 2022).
23. R. A. Brooks, R. Creiner, and T. O. Binford. International joint conference of artificial intelligence. In *Proceesings of the International Joint Conference of Artificial Intelligence*, pages 105–113, New York, NY, 1979. ACM.

## Acronyms

**AOI** Angle-of-Interest. 34

**AWGN** Additive White Gaussian Noise. 4

**CNN** Convolutional Neural Networks. 15

**dBm** milli-decibel. 12

**EM** Electromagnetic. 6

**EMOE** Electromagnetic Operating Environment. 1

**EMR** Electromagnetic Radiation. 5

**IADS** Integrated Air Defense. 1

**LO** Low Observable. iv

**MALD/J** Miniature Air Launch Decoy/Jammer. 2

**MOM-SEP** Method of Moments - Separation of Principles. 28

**PEC** Perfect Electrical Conductor. 6

**RADAR** Radio Detection and Ranging. 7

**RCS** Radar Cross Section. 4

**RNN** Residual Neural Network. 15

**SNR** Signal to Noise Ratio. 5

**TALD** Tactical Air Launch Decoy. 1

# REPORT DOCUMENTATION PAGE

*Form Approved  
OMB No. 0704-0188*

The public reporting burden for this collection of information is estimated to average 1 hour per response, including the time for reviewing instructions, searching existing data sources, gathering and maintaining the data needed, and completing and reviewing the collection of information. Send comments regarding this burden estimate or any other aspect of this collection of information, including suggestions for reducing this burden to Department of Defense, Washington Headquarters Services, Directorate for Information Operations and Reports (0704-0188), 1215 Jefferson Davis Highway, Suite 1204, Arlington, VA 22202-4302. Respondents should be aware that notwithstanding any other provision of law, no person shall be subject to any penalty for failing to comply with a collection of information if it does not display a currently valid OMB control number. PLEASE DO NOT RETURN YOUR FORM TO THE ABOVE ADDRESS.

<b>1. REPORT DATE (DD-MM-YYYY)</b> 19-03-2020	<b>2. REPORT TYPE</b> Master's Thesis	<b>3. DATES COVERED (From — To)</b> Sept 2018 — Mar 2020		
<b>4. TITLE AND SUBTITLE</b>  Thesis Title with a Second Line		<b>5a. CONTRACT NUMBER</b>  <b>5b. GRANT NUMBER</b>  <b>5c. PROGRAM ELEMENT NUMBER</b>		
<b>6. AUTHOR(S)</b>  Matthew M. Rofrano		<b>5d. PROJECT NUMBER</b>  <b>5e. TASK NUMBER</b>  <b>5f. WORK UNIT NUMBER</b>		
<b>7. PERFORMING ORGANIZATION NAME(S) AND ADDRESS(ES)</b>  Air Force Institute of Technology Graduate School of Engineering and Management (AFIT/EN) 2950 Hobson Way WPAFB OH 45433-7765		<b>8. PERFORMING ORGANIZATION REPORT NUMBER</b>  AFIT-ENG-MS-20-M-XXX		
<b>9. SPONSORING / MONITORING AGENCY NAME(S) AND ADDRESS(ES)</b>  AFXX/XXXX Building XXX WPAFB OH 45433-7765 DSN XXX-XXXX, COMM 937-XXX-XXXX Email: first.last@us.af.mil		<b>10. SPONSOR/MONITOR'S ACRONYM(S)</b>  XXXX/XXXX		
<b>11. SPONSOR/MONITOR'S REPORT NUMBER(S)</b>				
<b>12. DISTRIBUTION / AVAILABILITY STATEMENT</b>  DISTRIBUTION STATEMENT A: APPROVED FOR PUBLIC RELEASE; DISTRIBUTION UNLIMITED.				
<b>13. SUPPLEMENTARY NOTES</b>				
<b>14. ABSTRACT</b>  Short abstract paragraph text here.				
<b>15. SUBJECT TERMS</b>  subject terms here				
<b>16. SECURITY CLASSIFICATION OF:</b>  <b>a. REPORT</b> U <b>b. ABSTRACT</b> U <b>c. THIS PAGE</b> U		<b>17. LIMITATION OF ABSTRACT</b>  UU	<b>18. NUMBER OF PAGES</b>  XXX	<b>19a. NAME OF RESPONSIBLE PERSON</b> Captain First M. Last, AFIT/ENG
				<b>19b. TELEPHONE NUMBER</b> (include area code) (937) 255-3636, ext XXXX; first.last@afit.edu